Modeling background radiation using geochemical data: A case study in and around Cameron, Arizona

Kara E. Marsac [a,1], Pamela C. Burnley [a,*], Christopher T. Adcock [a], Daniel A. Haber [a], Russell L. Malchow [b], Elisabeth M. Hausrath [a]

[a] University of Nevada Las Vegas, Geoscience Department, 4505 S Maryland Parkway, Las Vegas, NV 89154, United States
[b] National Security Technologies, Aerial Measuring Systems, Remote Sensing Laboratory, PO Box 98521, Las Vegas, NV 89193, United States

ARTICLE INFO

ABSTRACT

This study compares high resolution forward models of natural gamma-ray background with that measured by high resolution aerial gamma-ray surveys. The ability to predict variations in natural background radiation levels should prove useful for those engaged in measuring anthropogenic contributions to background radiation for the purpose of emergency response and homeland security operations. The forward models are based on geologic maps and remote sensing multi-spectral imagery combined with two different sources of data: 1) bedrock geochemical data (uranium, potassium and thorium concentrations) collected from national databases, the scientific literature and private companies, and 2) the low spatial resolution NURE (National Uranium Resource Evaluation) aerial gamma-ray survey. The study area near Cameron, Arizona, is located in an arid region with minimal vegetation and, due to the presence of abandoned uranium mines, was the subject of a previous high resolution gamma-ray survey. We found that, in general, geologic map units form a good basis for predicting the geographic distribution of the gamma-ray background. Predictions of background gamma-radiation levels based on bedrock geochemical analyses were not as successful as those based on the NURE aerial survey data sorted by geologic unit. The less successful result of the bedrock geochemical model is most likely due to a number of factors including the need to take into account the evolution of soil geochemistry during chemical weathering and the influence of aeolian addition. Refinements to the forward models were made using ASTER visualizations to create subunits of similar exposure rate within the Chinle Formation, which contains multiple lithologies and by grouping alluvial units by drainage basin rather than age.

1. Introduction

1.1. Aerial gamma-ray surveys

Aerial gamma-ray surveys are one of the primary tools for tracking the dispersal of radioactive contamination in the environment (Pitkin et al., 1964; Sanderson et al., 1993; Lyons and Colton, 2012; Sanada et al., 2014) and are used for a variety of homeland security purposes as well as in disaster response and mitigation (cf. Blumenthal and Musolino, 2016; Blumenthal et al., 2103). For any gamma-ray survey made over land, a principal component of the naturally occurring radiological background comes from rocks and soils because earth materials inevitably contain some level of radionuclides, in particular potassium-40 (^{40}K), uranium-238 (^{238}U), thorium-232(^{232}Th) and their short-lived daughter products. During the recent disaster at the Fukushima Daiichi nuclear power plant in Japan, it became clear that for emergency response purposes, simple, rapid methods of separating the contaminant plume from natural background radiation coming from geologic sources are needed (Lyons and Colton, 2012). Past studies have focused on interpreting gamma-ray survey data in terms of bedrock or soil type (e.g. Griscom and Peterson, 1961; Pitkin et al., 1964; Galbraith and Saunders, 1983; Harris, 1989; Schetselaar and Rencz, 1997; Schetselaar et al., 2000; Wilford, 2002; Martelet et al., 2006; Rawlins et al., 2007; Dierke

* Corresponding author.
E-mail addresses: marsac@mymail.mines.edu (K.E. Marsac), Pamela.Burnley@unlv.edu (P.C. Burnley), adcockc2@unlv.nevada.edu (C.T. Adcock), haberd@unlv.nevada.edu (D.A. Haber), MalchoRL@nv.doe.gov (R.L. Malchow), elisabeth.hausrath@unlv.edu (E.M. Hausrath).
[1] Current address: Department of Civil and Environmental Engineering, 206 Coolbaugh Hall, 1012 14th St., Golden, CO 80401, United States.

and Werban, 2013; Beamish, 2013), prospecting for mineral resources (e.g. Dickson and Scott, 1997) or identifying fallout from nuclear weapons testing (Books, 1962). In contrast, our study attempts to use the measured geochemistry of the bedrock to forward model the observed natural gamma-radiation background. A successful method for modeling the background will be useful for a variety of homeland security, nuclear disaster response and resource exploration purposes. An ideal model would predict the gamma-radiation background point by point across the land surface, with each location modeled independently from each adjacent point. However, such a model would be impractical to construct. Instead, we seek to segment the region over which the model extends into geographic units over which average characteristics can be assigned. For the sake of discussion, we will refer to these geographic areas as 'background radiation units'. For reasons that will be apparent below, in this study we have chosen to define background radiation units using geologic maps and remote sensing imagery.

Airborne gamma-ray spectroscopy measures the gamma-radiation emitted at or near the surface of the Earth. Gamma-radiation is able to penetrate about 30 cm of rock or soil and a few hundred meters of air. ^{238}U, ^{40}K and ^{232}Th are the only naturally occurring radioactive isotopes that exist in large enough quantities, and produce gamma-rays (either directly or in their decay chains) with high enough energies to be measured during an aerial survey (Minty, 1997), which is typically conducted a few hundred meters off the ground. The energy released during radioactive decay is different for each isotope (Dickson and Scott, 1997). Potassium, a common element in rocks and soils, makes up approximately 2% of the Earth's crust. 0.012% of all potassium is its radioactive isotope, ^{40}K. Potassium is most abundant in K-feldspars and micas, and when these K-rich minerals are weathered the potassium may be incorporated into new clay minerals (Dickson and Scott, 1997). ^{232}Th is a radioactive isotope that occurs as a common trace element in rocks and soils, with a decay series that releases a number of gamma-rays that can be detected by aerial gamma-ray surveys. ^{232}Th itself does not release any high energy, high intensity gamma-rays; instead, its subsequent daughters release these gamma-rays which are used to calculate an equivalent Th (eTh) concentration. Th, with a crustal abundance of 12 ppm, occurs in significant quantities in minor minerals such as allanite, monazite, xenotime and zircon (Dickson and Scott, 1997). When Th is weathered out of a mineral, it tends to stay in place due to its low solubility. It can be taken up by clays or iron oxides (Koons et al., 1980), and if adsorbed by colloidal clays, can be transported out of the system. U is another important contributor to the gamma-radiation background. It occurs in many of the same environments, minerals, and rocks as Th when in its reduced state (U^{4+}). Unlike Th, U also has an oxidized state (U^{6+}) that is soluble and therefore mobile. Like ^{232}Th, ^{238}U does not release high energy, high intensity gamma-rays, but its daughters release these gamma-rays, which are used to calculate an equivalent U (eU) concentration. U occurs in the Earth's crust at a concentration of about 3 ppm, and has two major isotopes: ^{238}U and ^{235}U, with ^{238}U being far more abundant. U occurs in minor quantities in oxides and silicates and along grain boundaries, and in higher concentrations in zircon, monazite and xenotime (Dickson and Scott, 1997).

Disequilibrium can affect the decay series of U and Th, causing eU and eTh to differ from actual concentrations. eU is mainly calculated from the spectra of the ^{238}U daughter bismuth-214, while eTh is mainly calculated from the spectra of the ^{232}Th daughter thallium-208 (Minty, 1997). In a closed system, equilibrium occurs after 10 half-lives of the longest-lived daughter, which is about 40 years for Th and 1.5 million years for U (Dickson and Scott, 1997). Disequilibrium can also occur through the preferential removal of either the parent or daughter isotopes. Due to the low mobility of Th and its daughters in aqueous environments as well as the short half-lives of its daughters, the Th decay chain is less susceptible to disequilibrium. In contrast, due to the higher solubility of U^{6+} as well as the volatility of its daughter radon-222 (Rn), equilibrium in the U decay chain cannot be taken for granted. However, studies have shown that at least in arid environments, aerial gamma-ray survey interpretation is not affected by disequilibrium (Dickson, 1995).

1.2. Past studies

Aerial gamma-ray surveying of the US began in the late 1940s for the purpose of U exploration. With the advent of commercial nuclear power plants, aerial gamma-ray surveys of areas around nuclear facilities were employed to create a baseline against which to detect future anomalies (Pitkin et al., 1964). Even in these initial studies, the relationship between background radiation and bedrock geology was apparent. For example, Pitkin et al. (1964) proposed that faults could be detected by higher exposure rates due to leaking radon. Using an aerial gamma-ray survey done of the Maryland Piedmont, Griscom and Peterson (1961) found previously unknown mafic intrusions. Moxham (1963) concluded that surface radiation is dominated by contribution from rock, not soil in the northeastern US. Aerial gamma ray surveys are now used for a wide variety of applications including environmental monitoring (Jones, 2004; Sanderson et al., 2004), soils research (Beamish, 2013; Dierke and Werban, 2013), surficial processes research (Martz and deJong, 1990; Pickup and Marks, 2000) and as an aide to geologic mapping in remote areas (Campbell et al., 2007; Martelet et al., 2006; Ford et al., 2008) as well as for U, Th, and precious metals exploration (Mernagh and Miezitis, 2008; Dickson and Scott, 1997; Dickson, 1995; Wilford, 2002; Ford et al., 2007).

Although early studies measured radiation only in terms of counts per second, by the 1970s radiation was characterized in terms of exposure rate in units of μR/hr (micro-roentgen per hour). Exposure rate is a measure of ionizations in a mass of air generated by gamma-rays per unit of time. It can be determined by integrating the number of counts per second between approximately 0.4 MeV and 3.0 MeV. Using computational models of photon emission, Beck et al. (1972) and Løvborg and Kirkegaard (1974) proposed that exposure rates could be calculated from a linear combination of K, U, and Th concentrations. Grasty et al. (1984) compared the resulting coefficients to their own calculations and proposed average values of the coefficients, which have been cast in terms of dose by Duval et al. (2005) and used here assuming a factor of 0.1 between nGy/h and μR/h:

$$\dot{X} = 1.32 \, \text{K} + 0.548 \, \text{eU} + 0.272 \, \text{eTh} \tag{1}$$

Where $\dot{X}$ is exposure rate in μR/hr, K is weight percent potassium, eU is ppm uranium, and eTh is ppm thorium. From 1973 to 1980, the Atomic Energy Commission conducted an aerial gamma-ray survey of the continental United States known as the NURE (National Uranium Resource Evaluation) survey for the purpose of evaluating U resources (Duval et al., 2005). The data, made available by the USGS, are reported as K, eU and eTh concentrations, and exposure rates may be calculated using Equation (1).

Although relationships between bedrock geochemistry and the spatial distribution of exposure rates are widely observed, the relationship is not so straightforward that a gamma-ray survey can replace a geologic map. Average radioactive isotope contents for a wide variety of rock types have been determined (Mernagh and Miezitis, 2008; Dickson and Scott, 1997), but the ranges of radioactive isotope concentrations overlap (c.f. Fig. 6 in Beamish, 2013)

such that it is not possible to take the concentrations from an aerial gamma-ray survey and predict definitively what rock type is on the ground (Dickson and Scott, 1997). However, aerial gamma-ray surveys can be used to see boundaries between adjacent geologic units, and trends can be seen between radioelement content and rock type. (cf. Griscom and Peterson, 1961; Moxham, 1963; Pitkin et al., 1964; Dickson and Scott, 1997; Martelet et al., 2006; Rawlins et al., 2007; Ford et al., 2007, 2008; Beamish, 2013).

A number of factors and sources of radiation affect aerial gamma-ray surveys. In addition to gamma-radiation emitted by rocks and soils, background radiation from the equipment itself, cosmic radiation, and radon in the atmosphere and soil (Minty, 1997) also contribute to the spectra. The presence of absorbing material between the rocks and soil and the aerial detector remove radiation that would otherwise reach the detector. Background radiation from the aircraft, cosmic radiation, radon in the atmosphere and atmospheric attenuation are accounted for by a series of calibration procedures (IAEA TECDOC 1363, 2003). The effects of soil moisture and vegetation are more difficult to model. Therefore, for this study we chose to focus on an arid environment. Arid environments present their own complications, including alluvial and aeolian processes. Aeolian addition, an important process in the formation of arid desert soils, occurs when dust from regional and even global sources is deposited. The dust may have no relation to the chemistry of the bedrock it is deposited on. In temperate climates, soil is typically formed from the weathering of the bedrock it sits on, which is why the concentration of radioactive isotopes in soil is usually correlated to the concentration of radioactive isotopes in the bedrock (Pitkin et al., 1964; Beamish, 2013). Alluvial processes which are important in arid environments also impact the distribution of radioelements on the surface. For example, Books (1962) concluded that only generalizations can be made between bedrock geology and background radiation for an aerial gamma-ray survey of the Los Angeles area, because alluvium does not generally overlie its parent rock.

We focused on modeling background radiation from an area in north central Arizona, near Cameron, AZ (Fig. 1). Located in and around the Navajo Nation, this area was mined for U from the 1940s through the 1960s (Hendricks, 2001). The study area was chosen because a high resolution aerial gamma-ray survey was performed by the Remote Sensing Laboratory (a facility of the U.S. Department of Energy, National Nuclear Security Administration Nevada Operations Office) to assess the risk associated with exposure to radiation from mine tailings (Hendricks, 2001). The area has optimal conditions for aerial gamma-ray surveys: sparse vegetation and an arid environment.

The survey was conducted using two twin engine helicopters equipped with two detector pods each, containing between 8 and 12 2 × 4 × 16 inch thallium activated sodium iodide (NaI(Tl)) scintillation detectors. The altitude of the survey was 46 m above the terrain with a nominal footprint of 91 m (Hendricks, 2001). Flight lines were spaced 91 m apart in the east-west direction (Hendricks, 2001). Spectra were taken at one second intervals while traveling at an approximate airspeed of 40 m/s.

1.3. Geological context of the study area

The region around Cameron, AZ consists largely of gently dipping Permian and Triassic sedimentary rocks, partially obscured by Pleistocene and Pliocene basalt flows, overlain by Quaternary alluvial sediments, some of which are associated with the Little Colorado River and its tributaries (Fig. 2). The lowest part of the stratigraphic section outcrops in the southwest part of the study area where the Harrisburg Member of the Permian age Kaibab Formation (Pkh) occurs as a sandy limestone (Billingsley et al.,

2007), indicative of deposition in a gently sloping continental margin environment (Hopkins and Thompson, 2003). Going up section, a regional unconformity separates Pkh from the Triassic age Moenkopi Formation, which consists of distinctive red sandstone and siltstone beds, and thins from west to east in the study area (Billingsley et al., 2007). Ripple marks and flute casts in the Moenkopi Formation indicate a fluvial depositional environment. There are three members of the Moenkopi Formation in the study area (in ascending order): the Wupatki Member (TRmw), the Shnabkaib Member and lower massive sandstone member (undivided, TRmss), and the Holbrook and Moqui Members (undivided, TRmhm) (Billingsley et al., 2007). A regional unconformity separates TRmhm from the Triassic age Chinle Formation, the source of U mineralization in the study area. The Chinle Formation is divided into three members (in ascending order): the Shinarump Member and sandstone and siltstone member (undivided, TRcs), the Petrified Forest Member (TRcp), and the Owl Rock Member (TRco) (Billingsley et al., 2007). TRcs consists of predominantly sandstone, siltstone, and conglomerate deposited in a fluvial environment. The conglomerate is the source of the U, some of which is contained in petrified wood (Billingsley et al., 2007; Sigleo, 1979). This unit dominates the western portion of the study area and thins from west to east, sometimes pinching in and out. TRcp is a flood plain mudstone and fluvial sandstone unit (Dubiel, 1987), most prevalent in the eastern portion of the study area. TRco is a limestone and siltstone unit deposited in a lacustrine environment, with a small outcropping in the northeastern portion of the study area (Dubiel, 1987). These sedimentary rocks are capped by two basalt flows. The Black Point Basalt flows (Tbpb) occurring in the southwestern portion of the study area, are Pliocene age plagioclase-aphyric basalts (Billingsley et al., 2007), with a K-Ar age of 2.43 ± 0.32 Ma (Ulrich and Bailey, 1987). The Basalt flow of Tappan Wash (Qbt) is a clinopyroxene-olivine and alkali-olivine basalt of Pleistocene age (Billingsley et al., 2007), occurring in the northwest part of the study area, with a K-Ar age of 0.53 ± 0.19 Ma (Damon et al., 1974). Quaternary alluvial units in the study area are highly diverse and widespread, with types including: terrace gravels (QTg4, QTg5, Qg1, Qg2, Qg3), alluvial fans (Qa1, Qa2, Qa3), dunes (Qd, Qdb, Qdl, Qdp), aeolian deposits (Qae, Qes, Qsc), floodplain deposits (Qf), landslide deposits (Ql), stream channel deposits (Qs, Ts), valley fill (Qv), and others (Qps, Qtr). A single alluvial unit can be spread across the study area, with vastly different parent rock at each occurrence, making the composition highly heterogeneous and the geochemistry difficult to model. Dune units are perhaps the only units without these complications, as they represent small, isolated, sand dunes.

2. Methods

2.1. AMS data

The National Security Technologies, LLC (NSTec), Aerial Measuring System (AMS) section of the Remote Sensing Laboratory (RSL) provided us with a digital data set for the exposure rate map published in Hendricks (2001). Although the original spectral data has been lost, the data set does contain geolocated exposure rates. The AMS data and the geologic map were reprojected to the global coordinate system WGS 1984. The exposure rate data points were sorted by geologic unit using ERSI's ArcMap, creating background radiation units whose characteristics could be compared with model background radiation units. To minimize the possible effect of geolocation uncertainties, data points within 50 m of a geologic unit boundary were eliminated from the AMS data set. The footprint of an aerial gamma-ray survey conducted at 45 m above ground level is approximately 90 m in diameter, so data points
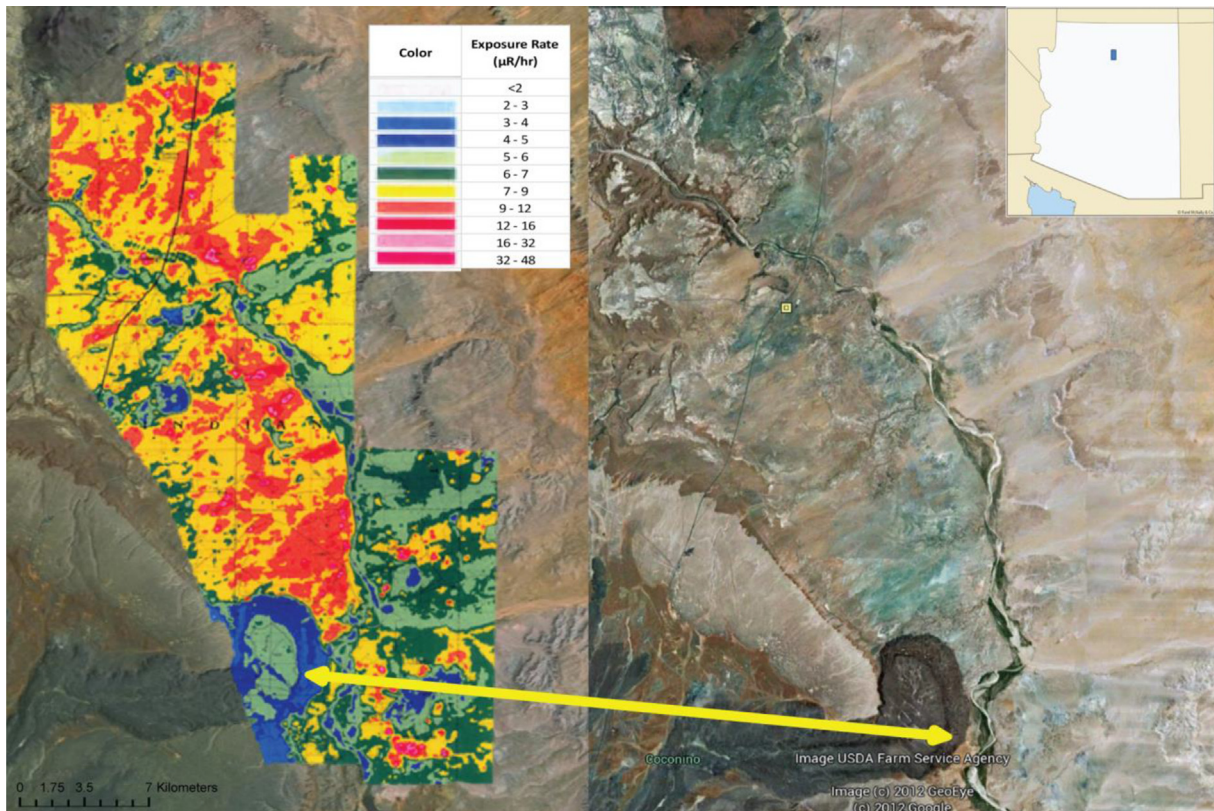
Fig. 1. Smoothed aerial gamma ray survey of the study area done by the Remote Sensing Laboratory (RSL) Aerial Measuring Systems (AMS) (left; Hendricks, 2001), satellite image (right; from USDA Farm Service). The study area is located in north central Arizona (a blue rectangle) as indicated in the sketch map of Arizona (inset). Clear correlation between bedrock geology and exposure rates can be seen in and around the basalt flow (yellow arrow).

within 50 m of a geologic boundary may have a significant contribution from more than one unit; the 50 m buffer zone mitigates this possible source of uncertainty. The mean, median, standard deviation and median absolute deviation (MAD) of exposure rate were calculated for each unit with and without buffer zones (Table 1). When the 50 m buffer zone was applied, one geologic unit, a small isolated dune unit, Qbd, lost all AMS data. However this unit also lacked geochemical data as well as NURE data (to be described below). Almost 50% of the AMS data was eliminated by adding the 50 m buffer zone. The use of the buffer zone lowered the average standard deviation of the AMS data sorted by geologic unit from 1.44 to 1.19 μR/h. We interpret the lower standard deviations to indicate that removing the buffer zone does remove data points that have contributions from more than one geologic unit, and thus are not representative of any single unit. Therefore, this realization of the AMS data set was used for all model comparisons unless otherwise noted.

An Analysis of Variance (ANOVA) statistical test was performed on the AMS data for each model created to assesses whether or not the variance within a set of background radiation units is more or less significant than the variance between the units. An F-Statistic is calculated by taking a ratio of the variance between the units and the variance within the units and compared to an F-Distribution with a 99% confidence interval (p-value of 0.01). The null hypothesis in this test states that the variance within the units is equal to or greater than the variance between the units and is likely to be true when the F-Statistic is less than the F-Critical value. The alternative hypothesis states that the variance within the units is less than the variance between the units and is likely to be true when the F-Statistic is greater than the F-Critical value. All models

discussed here have F-Statistics significantly higher than the F-Critical value leading to the conclusion that the null hypothesis may be rejected for all models.

Finally, a Chi Squared Goodness of Fit test was performed for each model, created with both geochemical and NURE data, to assess whether the predicted value is statistically similar to the observed value in the form of AMS data. The Chi Squared statistic is calculated by subtracting each observed and predicted value, squaring the result, and dividing by the observed value. These statistics are then summed and compared to a critical value derived from a Chi Squared distribution. The critical value chosen is the value for a 95% confidence interval (or p-value of 0.05). The null hypothesis states that the predicted and observed values are not significantly different and is true when the Chi Squared statistic is less than the critical value. The alternative hypothesis, which is true when the Chi Squared statistic is larger than the critical value, is that there is a significant difference between the predicted and observed values.

2.2. Geochemical sample data

In order to test the use of lab-based geochemical data to develop a background model, geolocated geochemical data containing U, K, and Th concentrations were obtained from the USGS and various publications through databases such as the Interdisciplinary Earth Data Alliance (IEDA) and the Geochemistry of Rocks the Oceans and Continents (GeoRoc) (Lehnert, 2016; Sarbas, 2008) and through DIR Exploration, a private U mining company (Table 2). The USGS data was accessed through the IEDA database, providing data mostly for alluvial units. These analyses vary in whether or not they include U,
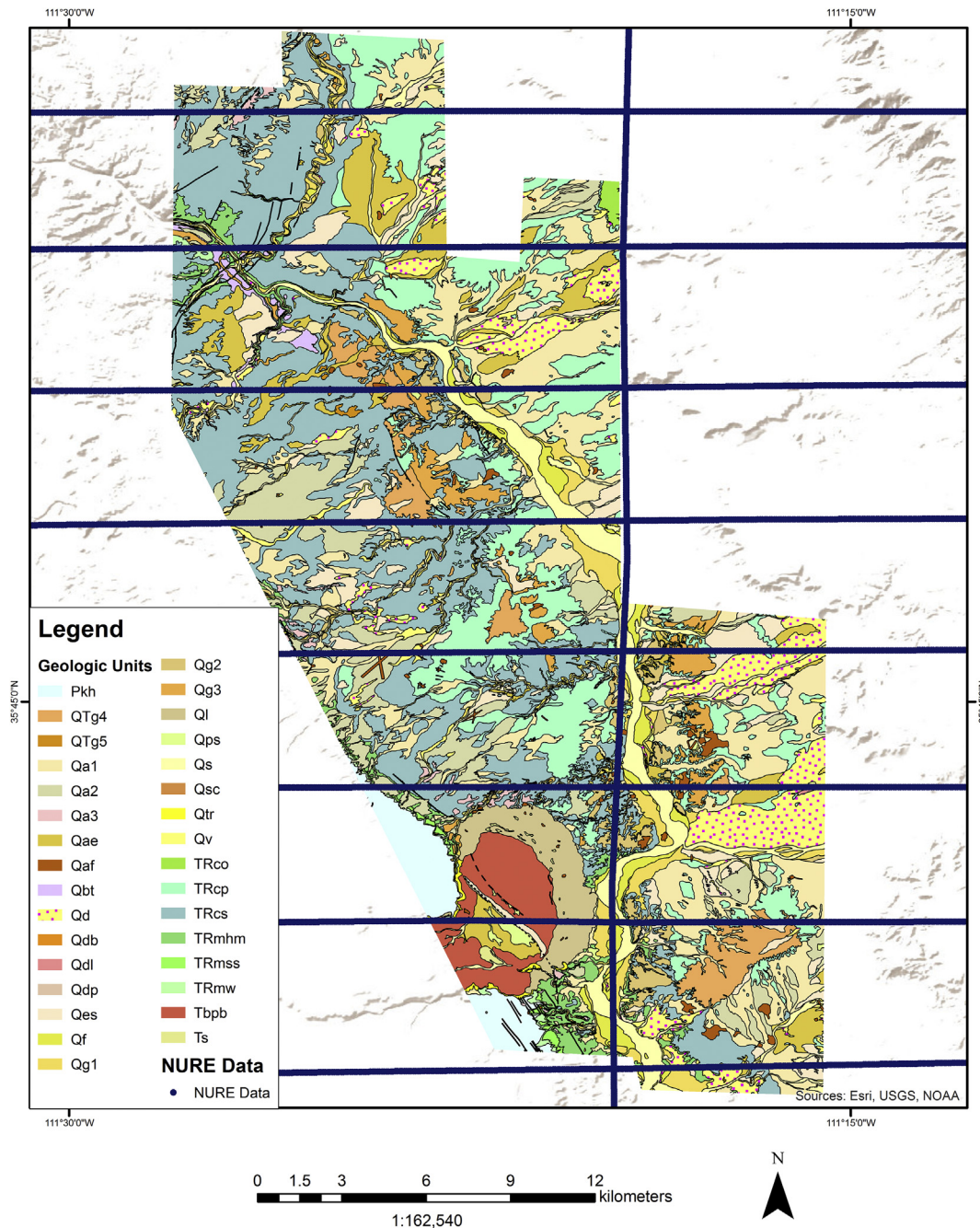
Fig. 2. Geologic map units (Billingsley et al., 2007) and distribution of National Uranium Resource Evaluation (NURE) aerial survey flight lines in study area (blue line). NURE data points are spaced at 100–200 ft along the flight line, so individual data points are not visible.

K and Th. GeoRoc yielded additional data points all of which were basalt analyses and included only K data. We also obtained geo-located data from a private uranium mining company, DIR Explo-ration, who provided geolocated U concentrations for rocks of unspecified type in our mapping area. The geochemical data were synthesized into a single data set and sorted with ArcMap by geologic unit based on its reported location and the 2007 USGS map (Billingsley et al., 2007). These data were then sorted and culled for internal consistency using the criteria discussed below. Regional bedrock geochemical data acquired outside the modeling area were included in the dataset if they were from a bedrock unit that also occurred in the modeling area. No alluvial unit data were brought into the dataset from outside the modeling area. The metadata

associated with each of the analyses provided by these databases varied greatly based on what the contributor chose to include; in many cases the rock type of the sample was not reported, and geologic units were rarely reported.

Data points were examined, and discarded or moved to an appropriate unit based on whether or not the description was consistent with the geologic unit assigned by location. If the author of the geochemical analysis stated that the sample was from a unit other than the one that occurred at its geolocation, it was moved to the author's specified unit. If the rock type of the data point was not consistent with the description of the geologic map unit (i.e., Billingsley et al., 2007), it was discarded. For samples that had multiple analyses using different methods, the geochemical data

Table 1
AMS data.

Geo unit	AMS aerial survey data sorted by geologic unit without 50 m buffer				AMS aerial survey data sorted by geologic unit with 50 m buffer			
	Average exposure rate (μR/hr)	Median exposure rate (μR/hr)	Std Dev	AMS MAD	Average exposure rate (μR/hr)	Median exposure rate (μR/hr)	Std Dev	AMS buffer MAD
Pkh	3.99	3.87	0.83	1.18	3.75	3.81	0.54	0.34
Qa1	8.36	7.95	1.99	1.77	8.20	7.85	1.81	0.24
Qa2	8.15	7.82	1.97	0.63	8.13	7.70	2.04	1.14
Qae	8.25	7.89	2.18	1.11	8.33	7.97	1.94	0.92
Qbt	6.39	6.54	0.91	1.09	6.86	6.71	0.76	1.38
Qd	7.00	6.64	1.10	0.58	6.86	6.59	0.95	1.23
Qes	7.50	7.23	1.62	1.83	7.43	7.08	1.56	0.26
Qf	7.06	7.03	1.30	1.08	7.04	7.01	0.98	2.08
Qg1	7.65	7.47	1.40	1.46	7.38	7.35	1.05	0.58
Qg3	7.64	7.19	1.80	0.48	7.50	6.98	1.71	0.42
Ql	4.61	4.55	0.82	6.22	4.49	4.47	0.48	0.38
Qs	7.12	6.80	1.73	1.68	6.29	6.01	1.03	1.47
Qv	8.29	8.30	1.50	1.19	8.21	8.34	1.42	1.69
Tbpb	5.72	5.83	0.61	1.84	5.83	5.93	0.55	1.01
TRcp	9.64	9.29	2.45	0.70	10.01	9.65	2.43	0.35
TRcs	9.44	9.35	2.09	0.10	9.47	9.43	1.98	1.57
TRmss	6.47	6.18	0.93	4.58	6.18	6.10	0.51	0.64
TRmw	7.35	7.39	1.51	0.08	7.98	8.13	0.94	0.05
Ts	5.81	5.82	0.17	0.19	5.80	5.82	0.11	0.20
QTg4	6.90	6.48	1.81	0.54	6.64	6.17	1.59	0.19
QTg5	7.63	7.67	1.17	1.91	7.61	7.47	0.98	2.19
Qg2	7.86	7.16	3.00	2.14	7.12	6.53	1.91	0.11
Qa3	8.11	8.35	1.35	0.26	7.81	8.01	1.36	0.92
Qdb	6.81	7.42	0.48	0.99				
Qdl	7.72	7.50	1.25	2.46	7.31	7.49	0.45	0.08
Qdp	7.71	7.50	1.22	2.87	7.76	7.78	1.59	1.57
Qtr	4.65	4.17	1.20	4.45	4.20	4.12	0.27	0.02
TRco	6.40	6.35	1.02	3.70	6.39	6.31	0.72	0.14
TRmhm	8.08	7.83	1.58	1.54	8.26	8.11	1.22	0.54
Qps	7.21	6.40	2.22	10.74	6.78	6.16	1.50	2.99
		Average:	**1.44**	**1.98**			**1.14**	**0.94**

Table 2
Geochemical data.

Geo unit	Number of data points	Mean U (ppm)	Median U (ppm)	Standard deviation U	Mean Th (ppm)	Median Th (ppm)	Standard deviation Th	Mean K (wt %)	Median K (wt%)	Standard deviation K
Pkh	184	185.26	1.45	1670.25	6.54	6.52	5.23	0.65	0.37	0.95
Qa1	18	37.02	1.80	88.12	11.90	11.90	1.27	0.93	0.88	0.51
Qa2	228	1.63	0.98	1.51	9.78	3.65	11.35	1.48	1.17	0.98
Qae	4	1.37	1.50	0.32				0.96		
Qbt	2							1.58		0.48
Qd	1							0.70		
Qes	1	1.50								
Qf	1	1.10								
Qg1	2	1.90						1.09		
Qg3	1	13.40			6.79			0.02		
Ql	7	4.64	6.38	3.19	24.43	32.20	18.51	1.62	0.91	1.38
Qs	8	1.71	1.60	0.59	1.40	1.40	1.84	0.26	0.10	0.37
Qv	63	1.62	1.40	0.95	4.78	4.78	4.21	0.56	0.31	0.49
Tbpb	4	0.78			2.74			0.91	0.91	0.02
TRcp	11	16.67	4.80	33.45	14.90	13.70	5.32	1.21	1.20	0.50
TRcs	6	14.95	5.14	21.76	17.53	15.70	7.92	1.59	1.30	1.27
TRmss	4	1088.52	40.90	2121.25	8.11		2.15	2.05	2.30	0.96
TRmw	3	421.57		591.76	33.95		25.67	2.11	2.30	0.45
TRco	1	2.94			4.90			1.60		
Total	**552**									

from the method with the smallest uncertainty was used (e.g. smaller neutron activation uncertainty vs larger atomic absorption spectroscopy uncertainty for U concentrations). Data assessment using these criteria left us with 530 geochemical data points out of over 1000 original data points. The majority of the data are associated with 2 geologic units: Pkh with 184 data points and Qa2 with 227. Table 2 gives the number of geochemical data points per unit. For the 2 bedrock units (TRmhm and Qbt) that did not have a full suite of associated U, K, and Th concentrations, average concentrations from an Australian geochemical survey (Dickson and Scott, 1997; Bruce Dickson, personal communication) and data from Mernagh and Miezitis (2008) who provide a table of average U, K, and Th concentrations for a variety of rock types were used to fill in these missing concentrations. For these units the concentration of the missing radioisotopes was approximated by taking an average of U, K and Th concentrations for all major rock types present in the
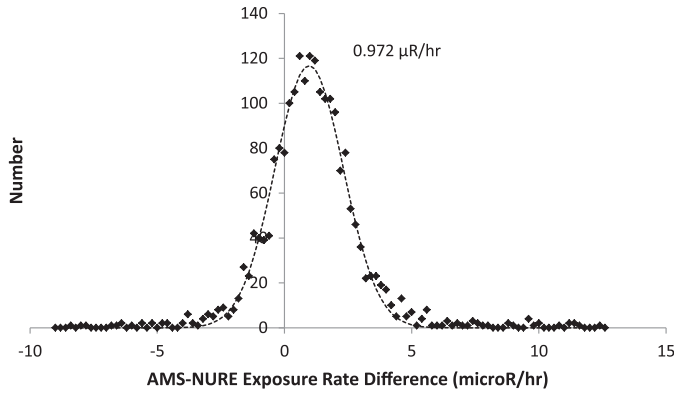
Fig. 3. Histogram displaying point to point comparison of AMS and NURE data. The NURE data has systematically lower exposure rates, thus a correction of 0.972 μR/h was applied to the NURE data.

unit based on the USGS description (i.e. Billingsley et al., 2007). The model for TRmhm (Holbrook and Moqui Members of the Moenkopi Formation) was created entirely from the data of the Australian survey. The second unit was a small volcanic unit, Qbt, for which we only had K concentrations, thus U and Th concentrations were estimated from the averages in Mernagh and Miezitis (2008). Ten alluvial units (which cover about 10% of the modeling area) had no associated geochemical data points and were therefore not included in the background model.

Mean, median, and standard deviation values were calculated for K, U and Th concentrations for each unit (Table 2). Mean values can be skewed by large outliers. This was particularly true for the mean U concentrations since this area hosts ore grade U concentrations, in some cases up to 17,000 ppm U. Thus median concentrations were used for the geochemical model. Exposure rates were calculated using Equation (1) in order to compare the geochemical model to aerial gamma-ray exposure rate data.

2.3. NURE data

NURE aerial survey data were obtained from the USGS compilation authored by Duval et al. (2005). The data are cast in the global coordinate system WGS 1984. In the study area there are 8 East/West NURE flight lines and 1 North/South flight line (Fig. 2). The survey reports K, eU, and eTh concentrations, thus Equation (1) was used to calculate an exposure rate for each data point. ArcMap was used to sort these data by geologic unit. A point to point comparison was made to examine whether there were systematic differences in AMS and NURE survey exposure rates, by comparing the AMS data point closest to each NURE data point. A histogram of the differences between the exposure rates of each pair of points is shown in Fig. 3. The histogram was fitted with a Gaussian distribution, yielding an average difference in exposure rate of 0.972 μR/h with a standard deviation of 1.91. This average difference was added as a correction to the NURE-based models to account for the systematic offset between the two aerial gamma-ray surveys. The resulting model is referred to as the NURE model. There are nine
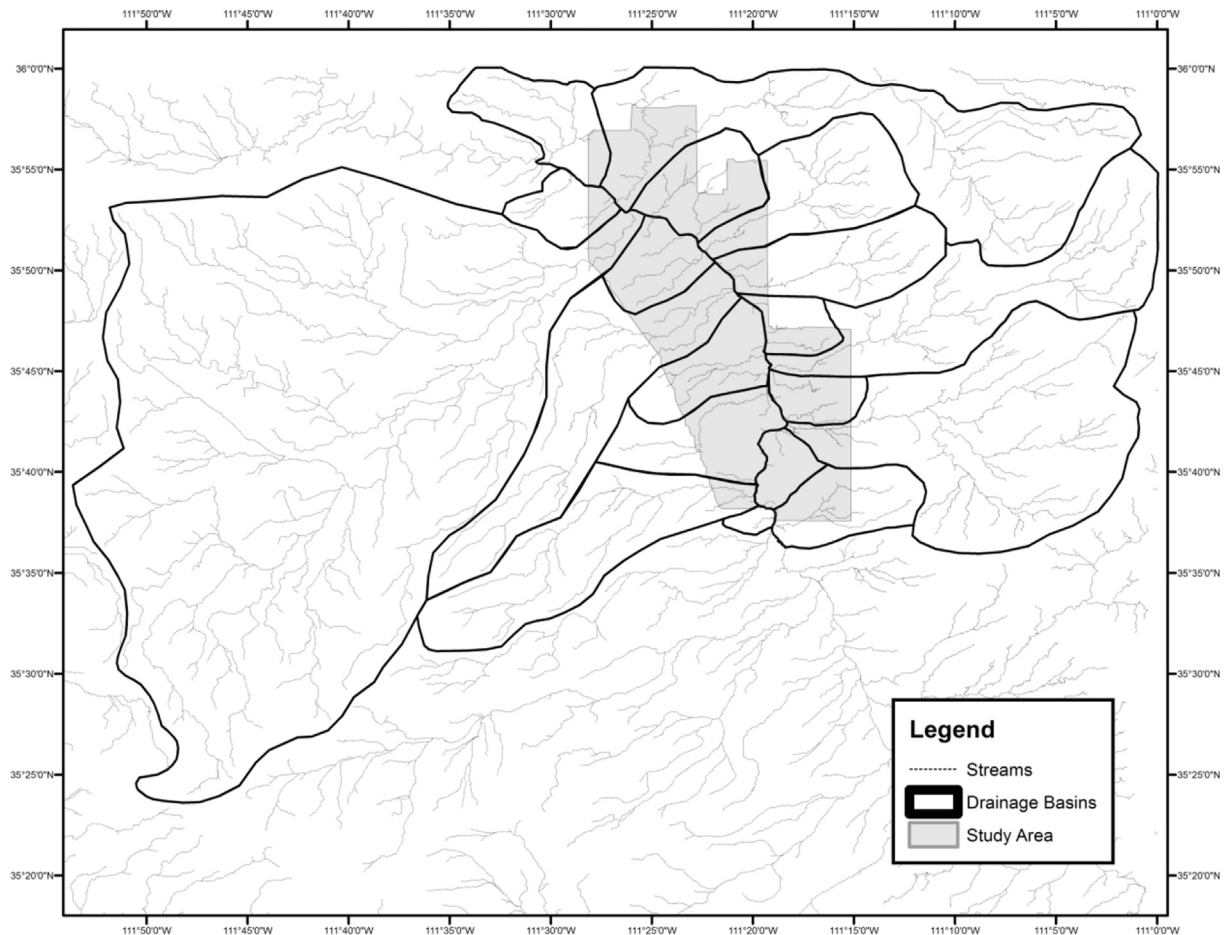

Fig. 4. Map of the Little Colorado River and its tributaries. Drainage basins that overlap the study area are outlined in black. The study area is indicated in grey.
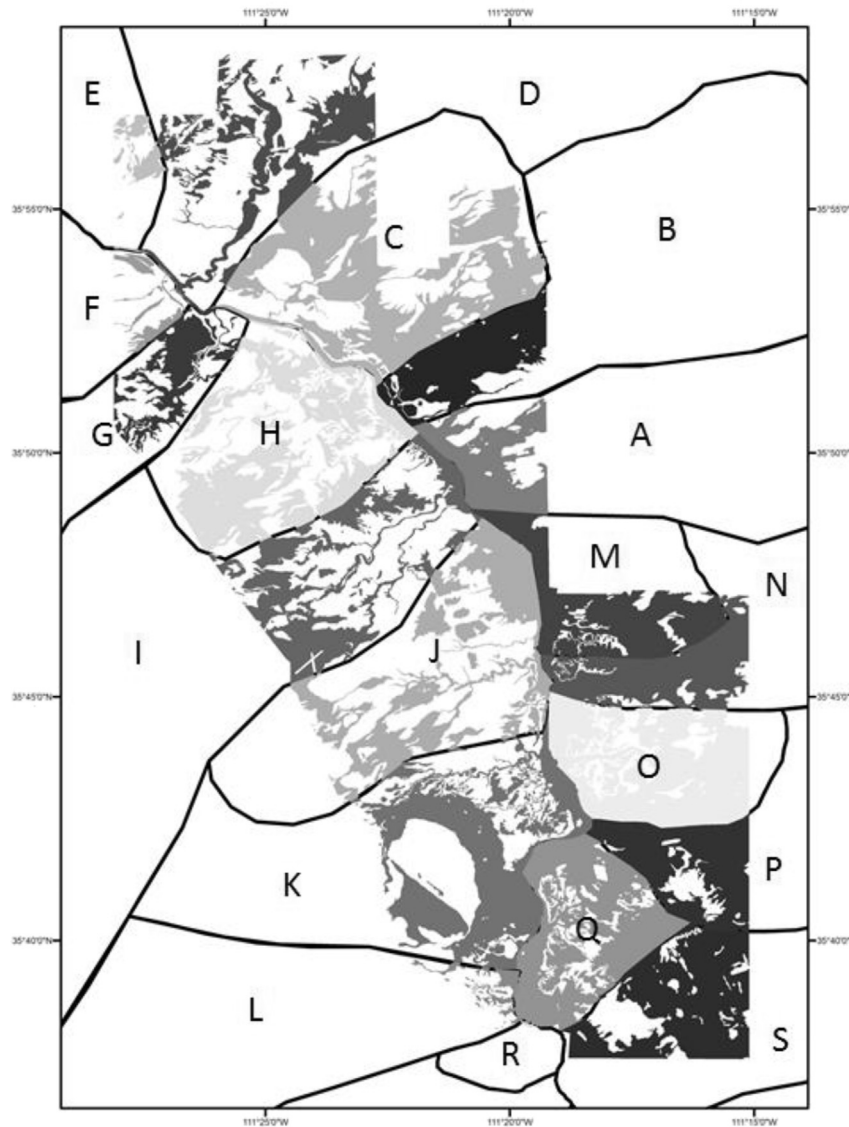
Fig. 5. Map of the 19 alluvial units (A–S) created by joining the alluvial units in each basin.

units with no NURE data: Pkh, TRmss, Ts, QTg5, Qa3, Qdb, Qdl, Qtr, and Qps. These units tend to have very small outcrops within the study area, and together make up only about 10% of the study area.

In order to create drainage basin models (described below under section Drainage Basins) NURE data were resampled for the entirety of the drainage basins and used to create three separate models. The first model includes all NURE data present in drainage basins (AN); the second model is all NURE data present in the drainage basins minus those over bedrock units located in the portion of the drainage basin that overlaps the study area; this model does however include data from bedrock units outside the study area as they may be significantly contributing to the alluvial deposits (ANNR); and the last model is NURE data over alluvial units only within the study area (SAONR).

2.3.1. Drainage basins

Alluvial units were modeled in 2 ways: by geologic unit and by drainage basin. Drainage basins for the Little Colorado River and its tributaries were manually drawn in ArcMap based on DEMs (Digital Elevation Models) (Fig. 4). Nineteen basins were identified (labelled

A through S), each representing a separate main tributary and all the streams in its headwater. Geologic units identified as alluvium within each drainage basin were joined into single alluvial units, resulting in 19 alluvial units (Fig. 5). AMS exposure rate data occurring within alluvial units were sorted into these 19 alluvial units to create a new standard, AMSDB (AMS Drainage Basin), to compare with NURE models created in the same way.

2.3.2. Remote sensing

The TRcs and TRcp members of the Chinle Formation, which cover much of the study area, consist of many different lithologies, including sandstone, limestone, conglomerate and mudstone. As can be seen in Table 1, both sedimentary units have large standard deviations in the AMS data. These rock types all have potentially different average K, U, and Th content, making it difficult to assign single K, U, and Th concentrations to these units. Therefore we experimented with using remote sensing techniques to subdivide the TRcs and TRcp units of the Chinle Formation.

Satellites, such as the Terra satellite, collect surface image data over a wide range of the electromagnetic spectrum, including UV,
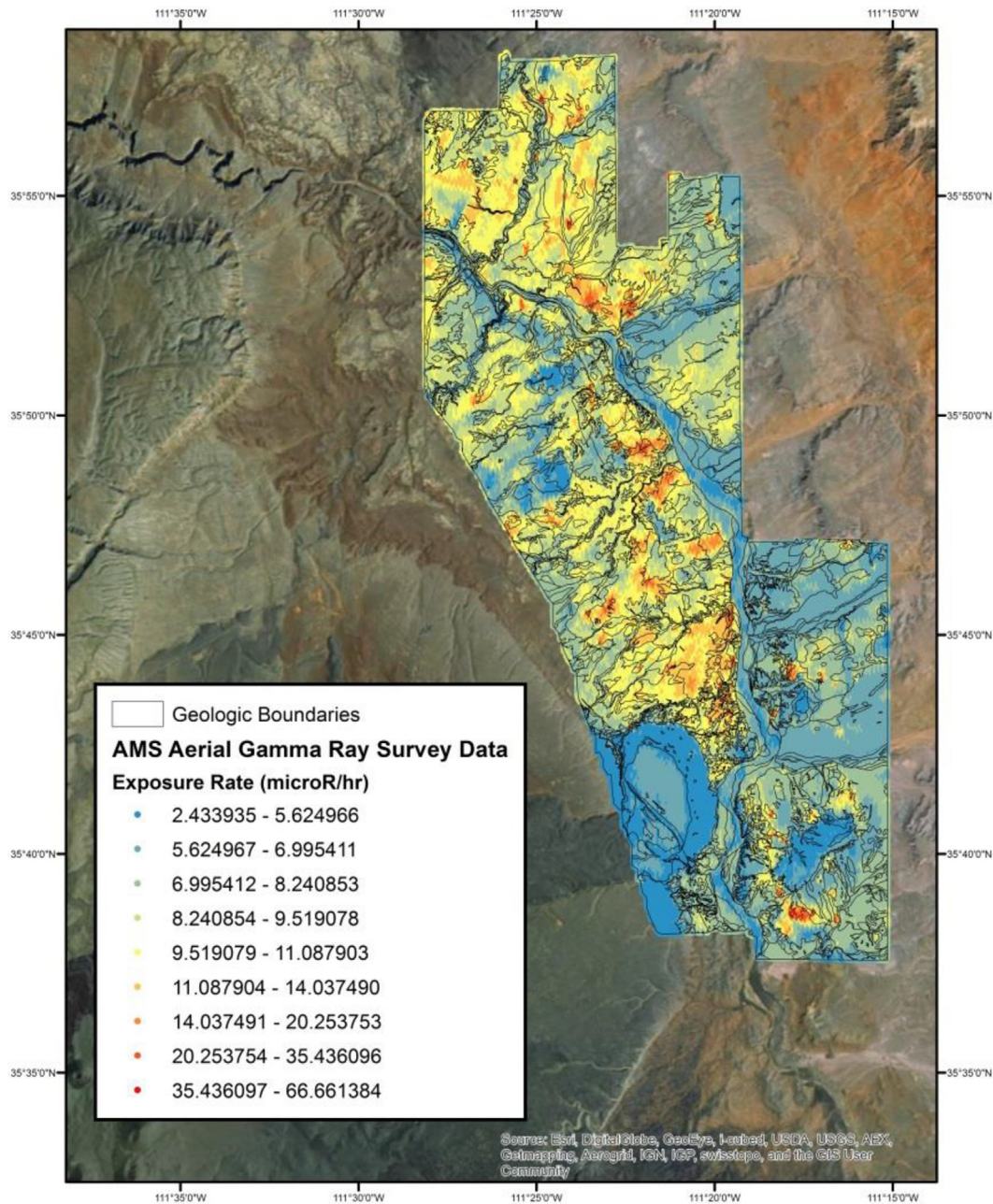
Fig. 6. The distribution of exposure rates over the study area measured by RSL AMS. Geologic boundaries are displayed for context. In contrast to Fig. 1 (from Hendricks, 2001) the data have not been smoothed.

visible, and infrared wavelengths. Data from the Advanced Space-borne Thermal Emission and Reflection Radiometer (ASTER), an instrument aboard Terra, were used to separate geologic units into mineralogically distinct subunits. The ASTER instrument collects data with 14 sensors (referred to as bands) that can detect narrow wavelength ranges in the visual, shortwave infrared, and thermal infrared wavelengths. Data from each of these bands can be used to highlight differences in mineralogy (van der Meer et al., 2012), as well as variations in thermal characteristics and vegetative cover. These differences in the image data were then used to develop a set of classes. The classes were used to subdivide the TRcp and TRcs units and create a model. Not all the classes contained data, so while 5 classes were created only the 4 with data are displayed in subsequent tables.

Publically available Level 1B ASTER data were acquired for daytime (image #AST_L1B_00306262007182049_20101006144116_21150) and nighttime (image #AST_L1B_00301182002053805_20101122202034_29129). False color composite (FCC) visualizations from ASTER were created by assigning image data of three bands to red, green, and blue color channels in images. Such FCC images have previously been used to distinguish differences in geologic surface units (e.g Rowan et al., 2003; Mars and Rowan, 2006; Chen et al., 2007; Di Tommaso and Rubinstein, 2007; Gad and Kusky, 2007; Pour and Hashim, 2012). We created FCC models using the following three-band combinations: bands 7-3-1 from the daytime ASTER image, which discriminate lithology (Abdeen et al., 2001); bands 2-6-10 from the

daytime data, a band combination we created to highlight clays and iron alteration based on observations of multiple band combinations over the Cameron area; and band combination 14-12-10 applied to the night time image, which is also used to discriminate lithologic units (McWilliam et al., 2005). In addition, we created grayscale image models by taking the ratio of the intensities of two ASTER bands from daytime data. We created models using the following band ratio images: 2/1 (where the numbers represent the ASTER band numbers), which highlights ferric iron on the surface (after Rowan et al., 2005); and 4/5, which highlights Fe- and Al-rich laterite-type soils (after Mars and Rowan, 2006). Finally, a FCC three band image was made by applying more complicated band math to daytime data: 2/1 (Red channel), (5 + 7)/6 (Green channel), and 13/12 (Blue channel). The band math combination (5 + 7)/6 was used to highlight clays and alteration (Mars and Rowan, 2006; Hewson and Cudahy, 2011) and band math combination 13/12 was used to discriminate quartz (Andrada de Palomera, 2002; Andrada de Palomera et al., 2015). Each visualization was first separated into five classes using the "Isocluster Classification" tool in ArcMap, and then polygonized in ArcMap and unioned with the Chinle formation geologic map to create five subunits for each of the Chinle's two main members, creating up to ten subunits in total. NURE data occurring in the Chinle Formation were sorted into these subunits to create new models for the Chinle Formation, which were compared to AMS survey data sorted into the same subunits. Remote sensing models based on geochemical data were not constructed, as there were not enough geochemical data points to populate all the subdivisions. We also made a model of the entire study area based on the 2-6-10 band FCC combination broken into ten classes for comparison with the model based on geologic map units.

## 3. Results

3.1. AMS data

The AMS measured exposure rate over the study area is shown in Fig. 6; in contrast to the map published by Hendricks (2001) (Fig. 1), the data are not smoothed. The mean and median AMS exposure rates calculated for each geologic unit are given in Table 1. The average of the standard deviations and MADs of AMS data separated into geologic units are 1.14 and 0.94 μR/h respectively. The ANOVA test F-Statistic is 1367.74 and compares to the F-Critical value of 1.70 (Table 3). The average exposure rate over geologic units from AMS data ranges from 3.75 μR/h to 10.01 μR/h. The lowest exposure rates for bedrock units are observed in Pkh (sandy limestone) and Tbpb (basalt), while the highest are observed in the Chinle formation members, TRcs and TRcp. Alluvial units vary in exposure rate, but units that are formed in the same way, such as the alluvial fan units Qa1, Qa2 and Qa3 tend to have similar exposure rates. The alluvial units with the lowest exposure rates are Qtr and Ql (which mostly occurs around Tbpb), while the highest exposure rates were observed in Qae and Qv.

Histograms of the AMS data for the majority of the geologic units display long exposure rate 'tails' (Fig. 7). The tails are likely due to the presence of U mineralization and the mobilization of U bearing materials by anthropogenic activities, which include the production of mine tailings, combined with both alluvial and aeolian processes. The mean exposure rate of each unit is skewed higher than the median exposure rate by these tails, in contrast to a symmetric dataset where the mean and median are the same.

For the AMS data sorted by the classified 2-6-10 visualization over the entire study area, unit exposure rates varied from 5.39 μR/h to 9.95 μR/h. The average of the standard deviations of AMS data separated by the remote sensing classes is 1.88 μR/h and the ANOVA

Table 3
F and Chi Statistics for each model.

Model	F-Stat	F-Crit	Chi squared	Chi Crit
NURE	1375.26	1.68	0.89	63.84
NURE Buffer	1367.74	1.70	1.08	31.41
Geochem Buffer	–	–	6912.80	23.68
2-6-10 All	3573.98	2.25	–	–
2-6-10 TRcp	511.05	3.32	0.37	5.99
2-6-10 TRcs	50.08	3.32	0.26	7.81
2d1 TRcp	145.35	2.80	0.41	9.49
2d1 TRcs	197.08	2.80	0.34	9.49
7-3-1 TRcp	169.38	2.80	0.66	7.81
7-3-1 TRcs	36.13	2.80	0.26	9.49
4d5 TRcp	43.48	3.32	1.13	9.49
4d5 TRcs	78.33	3.32	0.48	9.49
2D1-5A7D6-13D12 TRcp	609.94	3.32	1.23	9.49
2D1-5A7D6-13D12 TRcs	415.16	3.32	0.37	9.49
14-12-10 TRcp	236.12	3.32	1.13	9.49
14-12-10 TRcs	92.21	3.32	0.37	9.49
Basin AN	968.04	1.93	4.00	27.59
Basin ANNR	–	–	4.41	27.59
Basin SAONR	–	–	1.16	23.68
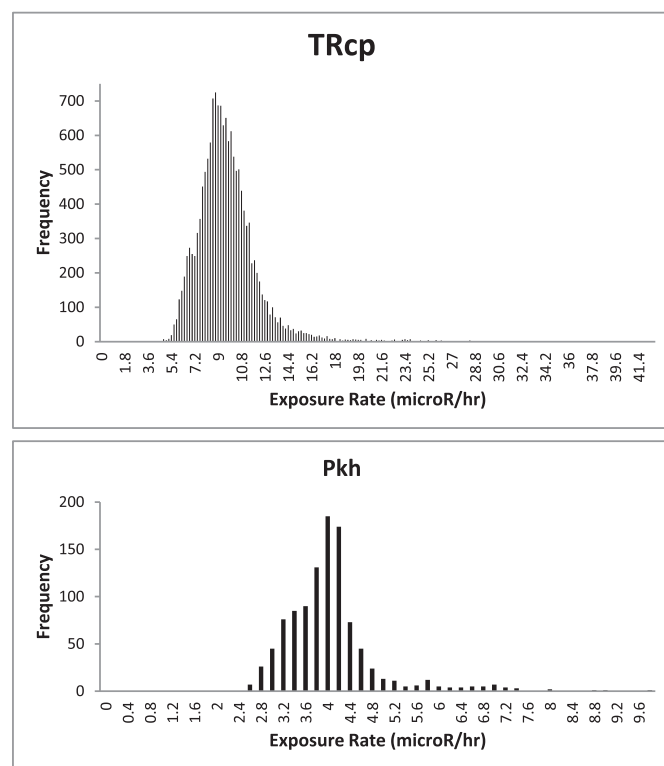
Fig. 7. AMS data for TRcp and Pkh. Both histograms display a significant tails towards high exposure rates.

test F-Statistic is 3574 compared to the F-Critical value of 2.25 (Table 3).

3.2. Geochemical model

Predicted exposure rates from the geochemical model range from 2.37 to 243 μR/h (Table 4). The difference between the median exposure rates predicted by the geochemical model and the AMS measured exposure rate ranged from 5.81 μR/h to −235.94 μR/h. The Chi Squared statistic for the geochemical model is 6912.8 and compares to the critical value of 23.68 (Table 3).

Table 4
Calculated exposure rate for geologic units from the Geochemical Model.
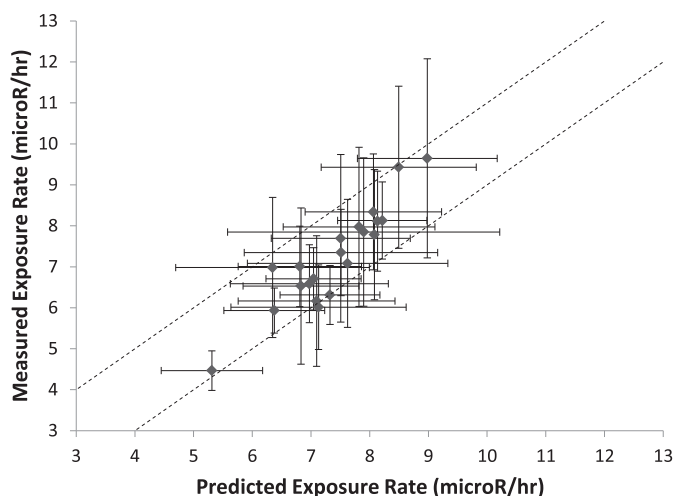
Geo unit	Median AMS buffer exp rate (μR/hr)	Geochemistry calculated exposure rate (μR/hr)	Difference (μR/hr)
Pkh	3.81	3.06	0.75
Qa1	7.85	5.28	2.57
Qa2	7.70	3.07	4.63
Qae	7.97		
Qbt	6.71	3.44[a]	3.27
Qd	6.59		
Qes	7.08		
Qf	7.01		
Qg1	7.35		
Qg3	6.98	9.22	−2.24
Ql	4.47	13.46	−8.99
Qs	6.01	1.77	4.24
Qv	8.34	2.48	5.86
Tbpb	5.93	2.37	3.56
TRcp	9.65	7.94	1.71
TRcs	9.43	8.80	0.63
TRmss	6.10	27.66	−21.56
TRmw	8.13	243.29	−235.16
Ts	5.82		
QTg4	6.17		
QTg5	7.47		
Qg2	6.53		
Qa3	8.01		
Qdb			
Qdl	7.49		
Qdp	7.78		
Qtr	4.12		
TRco	6.31	5.06	1.25
TRmhm	8.11	5.98[a]	2.13
Qps	6.16		

[a] These values were calculated using Dickson and Scott (1997), Dickson (personal communication) and Mernagh and Miezitis (2008).

Table 5
NURE model results.

Geo unit	Average AMS buffer exp rate (μR/hr)	Average NURE buffer exp rate (μR/hr)	Difference (μR/hr)	Median AMS buffer exp rate (μR/hr)	Median NURE buffer exp rate (μR/hr)	Difference (μR/hr)	AMS buffer Std Dev	AMS buffer MAD	NURE buffer Std Dev
Pkh	3.75			3.81			0.54	0.34	
Qa1	8.20	8.43	−0.22	7.85	7.90	−0.05	1.81	0.24	2.32
Qa2	8.13	7.59	0.54	7.70	7.51	0.19	2.04	1.14	1.18
Qae	8.33	7.68	0.66	7.97	7.82	0.15	1.94	0.92	1.29
Qbt	6.86	7.28	−0.42	6.71	7.04	−0.34	0.76	1.38	0.81
Qd	6.86	7.30	−0.44	6.59	6.97	−0.39	0.95	1.23	1.35
Qes	7.43	7.81	−0.38	7.08	7.62	−0.54	1.56	0.26	1.71
Qf	7.04	6.86	0.18	7.01	6.81	0.20	0.98	2.08	1.05
Qg1	7.38	7.77	−0.39	7.35	7.51	−0.16	1.05	0.58	1.65
Qg3	7.50	6.82	0.68	6.98	6.35	0.64	1.71	0.42	1.65
Ql	4.49	5.48	−0.99	4.47	5.31	−0.84	0.48	0.38	0.86
Qs	6.29	7.25	−0.96	6.01	7.13	−1.11	1.03	1.47	1.49
Qv	8.21	8.84	−0.62	8.34	8.06	0.28	1.42	1.69	1.16
Tbpb	5.83	6.15	−0.32	5.93	6.37	−0.44	0.55	1.01	0.86
TRcp	10.01	8.87	1.14	9.65	8.98	0.67	2.43	0.35	1.13
TRcs	9.47	8.51	0.96	9.43	8.49	0.94	1.98	1.57	1.32
TRmss	6.18			6.10			0.51	0.64	
TRmw	7.98	8.24	−0.26	8.13	8.21	−0.08	0.94	0.05	0.76
Ts	5.80			5.82			0.11	0.20	
QTg4	6.64	6.81	−0.17	6.17	7.10	−0.93	1.59	0.19	1.34
QTg5	7.61			7.47			0.98	2.19	
Qg2	7.12	6.94	0.18	6.53	6.83	−0.30	1.91	0.11	0.99
Qa3	7.81			8.01			1.36	0.92	
Qdl	7.31			7.49			0.45	0.08	
Qdp	7.76	8.08	−0.32	7.78	8.08	−0.30	1.59	1.57	
Qtr	4.20			4.12			0.27	0.02	
TRco	6.39	7.20	−0.81	6.31	7.32	−1.01	0.72	0.14	0.85
TRmhm	8.26	8.13	0.13	8.11	8.13	−0.02	1.22	0.54	
Qps	6.78			6.16			1.50	2.99	
		Average:	0.51			0.46	1.19	0.94	1.25

Fig. 8. Predicted exposure rate by the NURE model, versus the measured AMS exposure rate for each geologic unit. Error bars represent one standard deviation. The dashed lines are plotted at ± 1 $\mu R/h$ from the measured exposure rate.

3.3. NURE data based models

Values for the NURE model are reported in Table 5. Predicted exposure rates vary from 5.81 $\mu R/h$ to 8.9 $\mu R/h$. The NURE model had an average absolute difference in exposure rate from the AMS data of 0.51 $\mu R/h$ Fig. 8 shows the difference in exposure rate for each geologic unit. The average of unit standard deviations for the NURE model is 1.25 $\mu R/h$. The Chi Squared statistic for the NURE model is 1.08 and compares to the critical value of 31.41 (Table 3).

For alluvial units grouped by drainage basins three NURE models were tested: AN, ANNR, and SAONR. For the AN model the average of the absolute value of median exposure rate difference is 1.02 $\mu R/h$. Values for the AN model are reported in Table 6. The AN and ANNR models do not have a buffer zone applied to them, but are compared to the AMS data with a buffer zone. For the ANNR model the average absolute difference in median exposure rate is 1.06 $\mu R/h$. Values for the ANNR model are reported in Table 7. The average of the absolute differences in median exposure rate between the SAONR model and the AMS data with a buffer zone is

0.60 $\mu R/h$. Values for the SAONR model are reported in Table 8. The ANOVA test F-Statistic for the basin models is 968 compared to the F-Critical value of 1.93. The Chi Squared statistics for the basin models are all below the critical value and are reported in Table 3.

Values for remote sensing models of the Chinle Formation are reported in Tables 9 and 10. Fig. 9 is a comparison of AMS and NURE data for each remote sensing model. The ANOVA and Chi Squared test statistics, and critical values for the remote sensing models are reported in Table 3. The FCC remote sensing images and classified images are presented in the supplementary information.

4. Discussion

The goal of this study is to use preexisting geochemical data and geologic maps to predict exposure rate as measured in aerial gamma-ray surveys. In order for a background model to be useful it needs to predict the probability that the observed value is within a certain interval at a particular location. Thus the predictive background models can be evaluated on a variety of criteria: 1) how close the predicted average exposure rate over a given background radiation unit is to the measured average exposure rate; 2) how small the standard deviation or MAD of exposure rates, both predicted and observed, is over the background radiation unit to which the predicted average is applied; 3) how large the ANOVA test F-Statistic is relative to the F-Critical value; and 4) how large the Chi Squared statistic is relative to the Chi Critical value. With regard to the first criterion, our goal is to model the average exposure rate within ± 1 $\mu R/h$ of the observed exposure rate. With regard to the second and third criterion, we reason that if the standard deviation or the MAD of the exposure rate over a background radiation unit is smaller than the standard deviation or MAD of exposure rates over the larger region in which the background radiation unit sits, and the ANOVA test F-Statistic is much larger than the F-Critical value, then the background radiation unit has achieved some degree of homogeneity over a random division of the larger area into subunits. Thus, for example, we judge the sorting of exposure rate data for the entire area into geologic units to be superior to sorting the entire area by the 10 classes from the 2-6-10 image because the average of the unit standard deviations and MADs drop from 1.88 to 1.44 and 4.56 to 0.94 $\mu R/h$ respectively. As mentioned above, implementing a 50 m buffer zone on the geologic unit boundaries drops the average of the unit standard deviations to 1.14 $\mu R/h$.

Table 6
Basin AN model results.

Basin	Avg AMS buffer exp rate ($\mu R/hr$)	Avg AN exp rate ($\mu R/hr$)	Difference ($\mu R/hr$)	Median AMS buffer exp rate ($\mu R/hr$)	Median AN exp rate ($\mu R/hr$)	Difference ($\mu R/hr$)	AMS buffer Std Dev	AN Std Dev
A	7.22	7.33	−0.11	6.87	7.25	−0.38	1.20	1.62
B	6.95	7.20	−0.25	6.76	7.16	−0.40	0.87	1.57
C	9.23	8.48	0.75	8.86	8.39	0.47	2.37	1.17
D	8.74	6.06	2.68	8.47	5.68	2.79	1.86	1.73
E	9.14	10.51	−1.37	9.04	10.71	−1.67	0.61	1.80
F	7.64	6.28	1.36	7.67	5.52	2.15	0.88	2.28
G	7.46	5.48	1.98	7.50	5.31	2.19	0.76	1.44
H	7.50	7.73	−0.23	7.33	7.46	−0.13	1.39	1.65
I	8.49	6.06	2.43	8.10	5.63	2.47	1.95	1.76
J	9.09	8.27	0.82	8.82	8.79	0.03	2.39	2.87
K	5.62	7.33	−1.71	5.19	6.86	−1.67	1.58	2.27
L	6.94	4.88	2.06	7.28	4.87	2.41	1.04	0.77
M	6.62	7.06	−0.44	6.68	6.84	−0.16	0.68	1.36
N	6.66	5.62	1.04	6.51	5.40	1.11	0.68	1.50
O	7.05	7.04	0.01	6.70	6.74	−0.04	1.62	1.82
P	6.84	6.97	−0.13	6.92	6.90	0.02	0.84	1.39
Q	6.69	6.72	−0.03	6.64	6.50	0.14	1.39	1.26
R		6.91			7.01			1.09
S	7.57	7.15	0.42	7.27	7.23	0.04	3.23	1.05
		Average:	**0.99**			**1.02**	**1.41**	**1.60**

Table 7
Basin ANNR model results.

Basin	Avg AMS buffer exp rate (μR/hr)	Avg ANNR exp rate (μR/hr)	Difference (μR/hr)	Median AMS buffer exp rate (μR/hr)	Median ANNR exp rate (μR/hr)	Difference (μR/hr)	AMS buffer Std Dev	ANNR Std Dev
A	7.22	6.98	0.24	6.87	6.69	0.18	1.20	1.53
B	6.95	6.95	0.00	6.76	6.87	−0.11	0.87	1.57
C	9.23	8.39	0.84	8.86	8.34	0.52	2.37	1.24
D	8.74	5.94	2.80	8.47	5.60	2.87	1.86	1.63
E	9.14	10.58	−1.44	9.04	10.74	−1.70	0.61	1.79
F	7.64	5.84	1.80	7.67	4.95	2.72	0.88	2.18
G	7.46	5.48	1.98	7.50	5.30	2.20	0.76	1.43
H	7.50	7.98	−0.48	7.33	7.64	−0.31	1.39	1.75
I	8.49	5.77	2.72	8.10	5.45	2.65	1.95	1.53
J	9.09	7.67	1.42	8.82	8.09	0.73	2.39	3.54
K	5.62	6.90	−1.28	5.19	6.22	−1.03	1.58	2.25
L	6.94	4.88	2.06	7.28	4.87	2.41	1.04	0.77
M	6.62	7.08	−0.46	6.68	6.84	−0.16	0.68	1.38
N	6.66	5.62	1.04	6.51	5.40	1.11	0.68	1.50
O	7.05	7.00	0.05	6.70	6.78	−0.08	1.62	1.70
P	6.84	6.98	−0.14	6.92	6.91	0.01	0.84	1.39
Q	6.69	6.70	−0.01	6.64	6.50	0.14	1.39	1.21
R		6.91			7.01			1.09
S	7.57	7.09	0.48	7.27	7.19	0.08	3.23	1.07
		Average:	**1.10**			**1.06**	**1.41**	**1.61**

However, while the ANOVA test F-Statistic is very large for both models, suggesting both successfully break the surface up, the 2-6-10 model has a much larger statistic. This may be the result of the fact that there are fewer units broken out with the 2-6-10 image therefore making the variance between the units more significant.

4.1. Geochemical model

Only 15 geologic units had sufficient geochemical data to make a predictive model. With the exception of 2 units, all predicted exposure rates fell outside of our target range of ±1 μR/h (Table 4). In addition, the Chi Squared statistic is much larger than the critical value suggesting that the null hypothesis is not valid for this model. This could be due to a number of factors, but is most likely related to outliers, preferential sampling, lack of data, aeolian addition and other soil forming processes, and the spatial scale difference between aerial gamma-ray survey data points and the average rock sample size. While median concentrations were used to mitigate outliers, for units with less than five geochemical data points,

outliers had a large effect. For example, TRmw had three geochemical data points, but only two of the samples had U concentrations, one of which was 840 ppm, over two orders of magnitude higher than the crustal average of 3 ppm. This outlier U concentration leads to a model exposure rate of 243 μR/h, much higher than the average of the AMS data at 8.26 μR/h. Another factor that could explain units with much higher exposure rates than the AMS data (e.g. TRmw and TRmss) is a sampling bias: if sample collection was focused on U prospecting, samples of high U concentration are more likely to be in the databases. Geolocation errors may also have been a factor in the failure of the geochemical model to predict within ±1 μR/h. In particular, Qa2 has 225 samples that were recorded to have been collected in the exact same location. The USGS data is self-reporting and thus may not contain a sufficient number of recorded decimals in latitude and longitude, leading to uncertainty as to where a sample was actually collected. The data points that fell within Qa2 were of rock types that could reasonably have occurred in Qa2, and thus were not culled from the data set. However, in reality many of them may not have been

Table 8
Basin SAONR model results.

Basin	Avg AMS buffer exp rate (μR/hr)	Avg SAONR buffer exp rate (μR/hr)	Difference (μR/hr)	Median AMS buffer exp rate (μR/hr)	Median SAONR buffer exp rate (μR/hr)	Difference (μR/hr)	AMS buffer Std Dev	SAONR buffer Std Dev
A	7.22	8.54	−1.31	6.87	8.68	−1.81	1.20	1.10
B	6.95	7.73	−0.77	6.76	7.75	−0.99	0.87	1.15
C	9.23	8.39	0.84	8.86	8.34	0.52	2.37	1.25
D	8.74	8.05	0.70	8.47	8.01	0.46	1.86	1.02
E	9.14			9.04			0.61	
F	7.64	8.29	−0.65	7.67	8.29	−0.62	0.88	
G	7.46			7.50			0.76	
H	7.50	7.90	−0.40	7.33	7.60	−0.27	1.39	1.80
I	8.49	8.00	0.49	8.10	7.58	0.52	1.95	1.35
J	9.09	10.60	−1.50	8.82	9.29	−0.47	2.39	3.38
K	5.62	6.76	−1.14	5.19	6.59	−1.40	1.58	1.25
L	6.94			7.28			1.04	
M	6.62	6.88	−0.26	6.68	6.60	0.08	0.68	1.30
N	6.66	6.23	0.43	6.51	6.22	0.29	0.68	0.59
O	7.05	6.84	0.21	6.70	6.88	−0.18	1.62	0.81
P	6.84	6.25	0.59	6.92	5.69	1.23	0.84	1.34
Q	6.69	6.71	−0.02	6.64	6.58	0.06	1.39	1.21
R								
S	7.57	7.16	0.41	7.27	7.39	−0.12	3.23	1.03
		Average:	**0.65**			**0.60**	**1.41**	**1.33**

Table 9
TRcp remote sensing models.

Unit	% of data	Avg AMS exp rate (μR/hr)	Avg NURE exp rate (μR/hr)	Difference (μR/hr)	Median AMS exp rate (μR/hr)	Median NURE exp rate (μR/hr)	Difference (μR/hr)	AMS Std Dev	NURE Std Dev
TRcp		9.64	8.53	1.12	9.29	8.75	0.54	2.45	1.49
2-6-10									
TRcp2A	3.4	10.26	8.73	1.53	9.84	8.73	1.11	2.46	0.83
TRcp3A	0.0003	9.28			9.34			0.19	
TRcp4A	81.8	9.91	8.74	1.18	9.52	8.97	0.55	2.43	1.47
TRcp5A	14.8	7.82	7.78	0.04	7.46	7.86	−0.40	1.72	1.35
		Weighted Average:		**1.02**			**0.55**	**2.33**	**1.43**
2/1									
TRcp1B	25.4	10.00	8.76	1.23	9.76	8.97	0.79	1.75	1.32
TRcp2B	34.7	9.95	8.76	1.18	9.31	8.97	0.34	2.71	1.20
TRcp3B	27.6	9.45	8.66	0.79	9.05	8.92	0.13	2.63	1.54
TRcp4B	9.8	8.57	7.95	0.62	8.31	7.89	0.42	2.22	1.44
TRcp5B	2.5	7.87	7.83	0.04	7.31	7.94	−0.63	1.55	1.52
		Weighted Average:		**1.00**			**0.43**	**2.37**	**1.36**
7-3-1									
TRcp1C	2.1	10.41			9.74			2.67	
TRcp2C	13.1	10.32	8.53	1.78	9.98	8.66	1.32	2.26	1.63
TRcp3C	24.7	10.00	8.65	1.36	9.72	8.83	0.89	2.49	1.51
TRcp4C	30.8	9.83	8.58	1.25	9.39	8.92	0.47	2.48	1.62
TRcp5C	29.3	8.80	8.47	0.33	8.58	8.67	−0.09	2.23	1.35
		Weighted Average:		**1.05**			**0.56**	**2.38**	**1.48**
4/5									
TRcp1D	25.6	9.55	8.67	0.89	9.21	8.94	0.26	2.42	1.44
TRcp2D	21.7	9.36	8.36	1.00	9.04	8.55	0.49	2.32	1.40
TRcp3D	15.7	9.64	8.55	1.09	9.27	8.93	0.34	2.41	1.47
TRcp4D	18.5	9.50	8.23	1.27	9.21	8.43	0.78	2.29	1.35
TRcp5D	18.4	10.15	8.84	1.31	9.92	9.07	0.85	2.74	1.45
		Weighted Average:		**1.09**			**0.53**	**2.43**	**1.42**
2/1-(5 + 7)/6-13/12									
TRcp1E	26.9	8.89	8.74	0.15	8.66	8.94	−0.28	1.96	1.12
TRcp2E	21.9	9.62	8.39	1.22	9.42	8.68	0.74	1.71	1.51
TRcp3E	14.4	8.32	7.65	0.67	7.71	7.31	0.40	2.57	1.58
TRcp4E	12.3	10.44	9.14	1.30	10.18	9.30	0.88	2.50	1.27
TRcp5E	24.5	10.89	8.95	1.94	10.43	9.08	1.36	2.70	1.79
		Weighted Average:		**1.04**			**0.74**	**2.24**	**1.45**
14-12-10									
TRcp1F	25.1	8.77	7.83	0.94	8.19	7.88	0.31	2.62	1.54
TRcp2F	35.4	9.68	8.47	1.21	9.39	8.53	0.86	2.14	1.70
TRcp3F	23.4	10.22	9.22	0.99	9.90	9.22	0.68	2.33	1.10
TRcp4F	11.4	10.36	8.86	1.50	9.93	9.01	0.92	2.76	1.00
TRcp5F	4.7	8.84	8.88	−0.03	8.70	8.82	−0.12	1.21	0.95
		Weighted Average:		**1.07**			**0.65**	**2.32**	**1.40**

properly located. The database also provides no way of connecting data points with published work, making it impossible to perform checks based on unit names and descriptions, mapped sample locations or even to contact authors. These geolocation errors may therefore have also been a factor for other geologic units as well.

For many geologic units, the geochemical model under predicted exposure rate, which points to additional sources of error. For example, unit Tbpb, a Quaternary basalt flow, has a higher exposure rate than is predicted by its chemical analysis. The geochemical data are consistent with the chemical analyses of basalts and the flow is a large enough feature that geolocation errors are not likely to be a factor. One possible explanation is that weathering processes and the addition of an aeolian dust increases the exposure rate of the soil developed on the basalt.

Another challenge in using geochemical data is unit heterogeneity. The aerial gamma-ray survey (with the aircraft at 45 m above ground level) measures the average exposure rate over a footprint of ~6500 m² (Hendricks, 2001). If either the bedrock or soil has chemical heterogeneity on that scale, a small number of hand sample analyses may not be representative of the chemistry of the footprint, let alone the unit as a whole. For example, for Pkh (a

limestone and sandstone unit) we were able to model the exposure rate to within 0.93 μR/h. This is most likely due to the fact that there were 184 data points within this unit, so the variation within the unit was fully sampled (Fig. 7).

Alluvial units are difficult to model based on geochemical sample data because of the highly heterogeneous nature of most alluvial units. With clast sizes ranging over five to six orders of magnitude, we expect that a statistically significant sampling of an alluvial fan might require a sample size three to four orders of magnitude larger than the typical geochemical sample size. Alluvial units are also categorized by age and how they were formed, so many alluvial units occur dispersed across the study area and may therefore originate from parent rocks with a variety of different compositions.

4.2. NURE data based models

The most successful models were based on the NURE aerial gamma-ray survey data set sorted into geological units (NURE model) (Table 5). This success is no doubt in part because aerial gamma-ray survey data are being compared to aerial gamma-ray

Table 10
TRcs remote sensing models.

| Unit	% of data	Avg AMS exp rate (μR/hr)	Avg NURE exp rate (μR/hr)	Difference (μR/hr)	Median AMS exp rate (μR/hr)	Median NURE exp rate (μR/hr)	Difference (μR/hr)	AMS Std Dev	NURE Std Dev
TRcs		9.44	8.77	0.67	9.35	8.67	0.54	2.09	1.60
2-6-10									
TRcs2A	20.8	9.54	8.73	0.83	9.55	8.46	1.09	2.46	0.83
TRcs3A	0.2	9.16	8.20	0.96	8.89	8.20	0.69	0.19	
TRcs4A	76.8	9.39	8.74	0.58	9.33	8.78	0.55	2.43	1.47
TRcs5A	2.3	8.40	7.78	1.08	8.37	7.45	0.92	1.72	1.35
		Weighted Average:		**0.64**			**0.67**	**2.42**	**1.33**
2/1									
TRcs1B	1.4	9.57	8.88	0.69	9.36	8.65	0.71	2.22	0.99
TRcs2B	16.0	10.05	8.94	1.10	9.70	8.84	0.86	2.88	1.46
TRcs3B	30.6	9.67	9.39	0.29	9.56	9.30	0.26	2.02	1.51
TRcs4B	32.4	9.19	8.56	0.64	9.24	8.44	0.80	1.73	1.53
TRcs5B	19.58	8.81	7.79	1.02	8.90	8.00	0.90	1.70	1.49
		Weighted Average:		**0.68**			**0.66**	**2.00**	**1.50**
7-3-1									
TRcs1C	20.5	9.40	8.46	0.93	9.43	8.35	1.08	1.44	1.35
TRcs2C	31.4	9.33	8.84	0.48	9.38	8.83	0.55	1.63	1.47
TRcs3C	28.4	9.22	8.57	0.65	9.24	8.58	0.66	1.88	1.42
TRcs4C	13.7	9.88	9.10	0.79	9.52	8.88	0.64	2.93	2.01
TRcs5C	6.0	9.60	9.01	0.59	9.12	8.49	0.63	3.68	1.85
		Weighted Average:		**0.67**			**0.71**	**1.96**	**1.53**
4/5									
TRcs1D	22.0	9.39	8.91	0.48	9.34	9.03	0.31	2.26	1.26
TRcs2D	17.9	9.09	8.21	0.88	9.06	8.17	0.90	1.91	1.26
TRcs3D	15.1	9.42	8.66	0.76	9.36	8.57	0.80	2.03	1.42
TRcs4D	14.8	9.17	8.25	0.92	9.14	8.08	1.06	2.33	1.92
TRcs5D	30.2	9.72	9.18	0.54	9.59	9.06	0.53	1.90	1.68
		Weighted Average:		**0.68**			**0.67**	**2.06**	**1.51**
2/1-(5 + 7)/6-13/12									
TRcs1E	10.5	9.27	8.78	0.49	9.26	8.55	0.71	1.65	1.96
TRcs2E	5.1	9.59	8.71	0.88	9.37	8.66	0.71	2.02	1.12
TRcs3E	32.8	8.67	7.87	0.80	8.76	8.00	0.76	1.71	1.44
TRcs4E	28.5	10.01	8.97	1.04	9.80	8.67	1.13	2.29	1.32
TRcs5E	23.1	9.36	9.27	0.08	9.33	9.25	0.08	2.29	1.75
		Weighted Average:		**0.67**			**0.70**	**2.02**	**1.52**
14-12-10									
TRcs1F	8.1	9.21	8.14	1.07	8.57	8.07	0.51	4.02	1.34
TRcs2F	13.4	8.95	8.81	0.14	8.92	8.95	−0.03	1.70	2.46
TRcs3F	30.8	9.27	8.58	0.69	9.24	8.58	0.66	2.20	1.38
TRcs4F	30.0	9.64	9.01	0.63	9.55	8.89	0.65	1.46	1.38
TRcs5F	17.7	9.67	8.92	0.76	9.66	8.38	1.29	1.58	1.50
		Weighted Average:		**0.64**			**0.67**	**1.95**	**1.54**

survey data, so factors such as vegetative cover and the geochemistry of the soil are included in both datasets. The overall average difference between the NURE model and the AMS data was 0.51 μR/h for the unit means, while the average difference of the medians was 0.46 μR/h (Table 5). As mentioned above, the distribution of exposure rates within most of the units in the study area has a significant skew towards higher exposure rates. The median is less sensitive to whether the high exposure rate tail is fully characterized, and thus we have focused our analysis on median values (Table 11).

Drainage basin models of the alluvial units were not as successful as models based on geologic units in this location, but could be a viable option in other study areas. The best basin model was the SAONR model, which included the least amount of data. The average difference between the SAONR model and the AMS model is 0.60 μR/h, in comparison to 0.428 μR/h for alluvial units based on the geologic map. This is most likely the best basin model because AMS and NURE data are being compared for the same areas, whereas the ANNR model and the AN model include data from outside the study area where there are no AMS data. In addition, the SAONR model has the lowest Chi Squared statistic compared to the other basin models.

As mentioned above, the TRcp and TRcs geologic units of the Chinle Formation contain lithologic subunits and have higher standard deviations than other background radiation units based on geologic units (Table 9). The same criteria for judging success of the other predictive models can be applied to the remote sensing models; specifically, the difference between the exposure rate means, the size of the standard deviations and the ANOVA test F-Statistic. In addition, the ability of the models to achieve some degree of separation into units with distinctive geographic separation and exposure rates is important.

The 2-6-10 FCC image (Supplement Fig. 1) was chosen as a basis for a model because it visually appeared to discriminate the sublithologies of the study area, especially in alluvial units. Band 2 (Red hues) can highlight the Fe^{+3} iron oxidation state which can be associated with weathering products (Rowan and Mars, 2003). Band 6 (applied to the green in the image) is often used in band math involving the study of weathered materials such as clays. Clays can hold and concentrate K+. Th, though poorly soluble, can be taken up by, and reside within, Fe-oxides and clays (Koons et al., 1980). Band 10 (blue hues) is in the thermal infrared range. In this
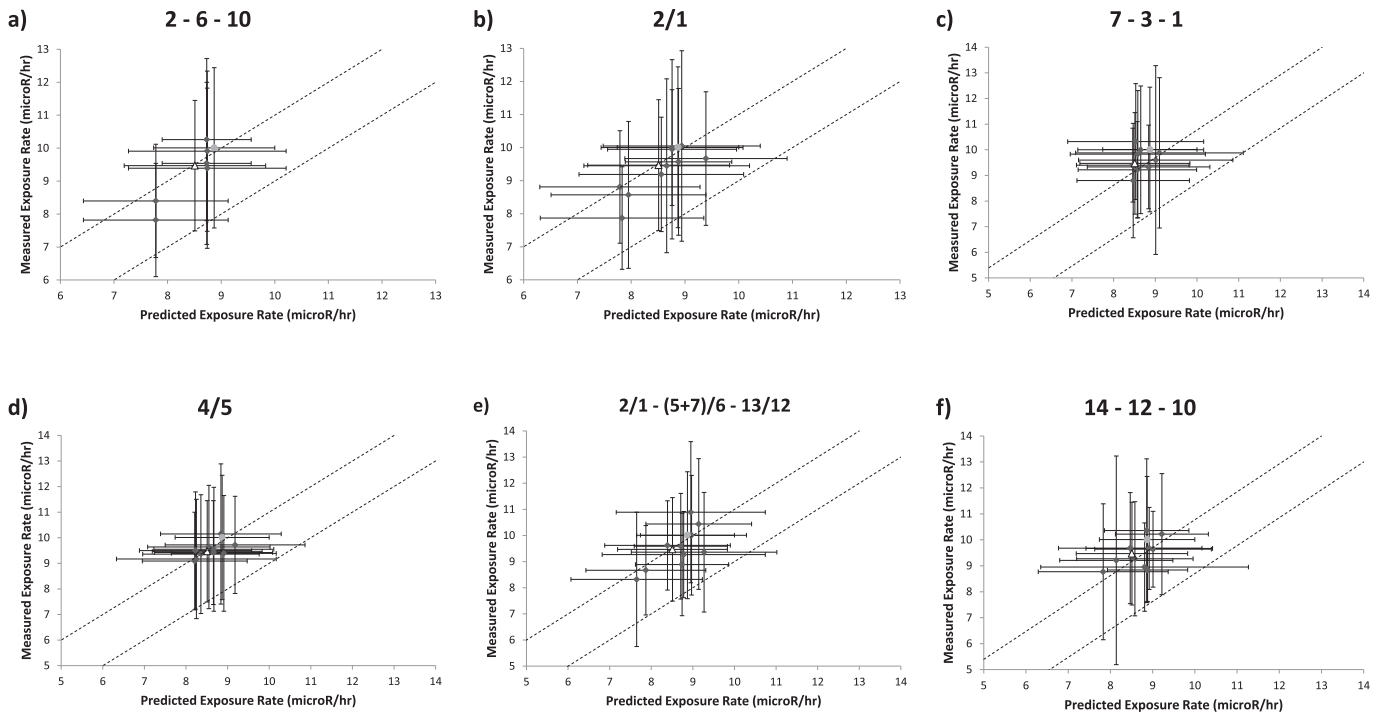
Fig. 9. Predicted exposure rates by the NURE model, versus the measured AMS exposure rate for each remote sensing model. Error bars represent one standard deviation. Grey circle is TRcp from the NURE model, white triangle is TRcs from the NURE model. The dashed lines are plotted at ±1 μR/h from the measured exposure rate. a) 2-6-10 ASTER model b) 2/1 ASTER model c) 7-3-1 ASTER model d) 4/5 ASTER model e) 2/1−5 + 7/6−13/12 ASTER model f) 14-12-10 ASTER model.

range, bedrock and unconsolidated materials (i.e. sediments and sand) can give very different signals. Thus the 2-6-10 image should discriminate differing subunits which have implications for gamma-ray exposure rates. The classification model based on the 2-6-10 image successfully distinguishes the TRcp and TRcs geologic units. However, the model does not make full use of the classes; ~80% of all data points for both TRcs and TRcp are in one class (Tables 9 and 10). For the other remote sensing models, data are more evenly distributed across the classes and no one class

contains more than ~35% of the data. For the 2-6-10 model both weighted averages of the standard deviations and the differences between the AMS and NURE data are worse for TRcs than for that unit undivided. For TRcp the weighted averages of the standard deviations and the differences between the AMS and NURE data are similar to that for the undivided unit. The ANOVA test F-Statistic for the 2-6-10 TRcs and TRcp models are 50 and 511 respectively further highlighting this relationship.

The 2/1 band ratio is used for distinguishing ferric iron (Fe^{+3}) (Rowan and Mars, 2003). Ferric iron, the more oxidized form, is associated with weathered materials and is part of colloidal Fe-oxyhydroxides which can be associated with clays. The 2/1 band ratio can highlight differences in weathering and also source between alluvial units (Supplement Fig. 2). For the 2/1 model, the weighted standard deviations are slightly smaller than for the undivided units and the ANOVA test F-Statistics are similar for both TRcp and TRcs. The difference between the predicted and observed mean exposure rate is smaller for TRcp but larger for TRcs. The model achieves the third and second largest degree of separation between exposure rates of the subunits for TRcp and TRcs, respectively (See Fig. 9).

For both the 7-3-1 and 4/5 remote sensing models (Supplement Figs. 3 and 4), the degree of separation between exposure rates of the subunits is substantially smaller than that achieved by the 2/1 model. The weighted standard deviations of the subunits are quite similar to the undivided TRcp and larger than that for the undivided TRcs, and the ANOVA test F-Statistics, while much higher than the critical value, are low relative to other models. The difference between the AMS and NURE data for the subunits within these models are either comparable or greater than they are for the undivided unit. This is also the case for the 14-12-10 FCC using nighttime image data (Supplement Fig. 5).

The 2/1-(5 + 7)/6-13/12 model (Supplement Fig. 6) creates the largest separation between exposure rates within the subunits as

Table 11
Summary of NURE-based models.

Model	Difference (μR/hr)	AMS Std Dev	NURE Std Dev
NURE Model Alluvial units	0.46	1.19	1.25
Geologic map	0.43	1.30	1.39
AN	1.02	1.41	1.60
ANNR	1.06	1.41	1.61
SAONR	0.60	1.41	1.33
TRcp			
TRcp undivided	0.54	2.45	1.49
TRcp 2-6-10	0.55	2.33	1.43
TRcp 2/1	0.43	2.37	1.36
TRcp 7-3-1	0.56	2.38	1.48
TRcp 4/5	0.53	2.43	1.42
TRcp 2/1-(5 + 7)/6-13/12	0.74	2.24	1.45
TRcp 14-12-10	0.65	2.32	1.40
TRcs			
TRcs undivided	0.54	2.09	1.60
TRcs 2-6-10	0.67	2.42	1.33
TRcs 2/1	0.66	2.00	1.50
TRcs 7-3-1	0.71	1.96	1.53
TRcs 4/5	0.67	2.06	1.51
TRcs 2/1-(5 + 7)/6-13/12	0.70	2.02	1.52
TRcs 14-12-10	0.67	1.95	1.54

the ANOVA test F-Statistics supports (610 for TRcp and 415 for TRcs). However, for the majority of the subunits the difference between the AMS and model exposure rates are larger than for the undivided units.

Generally, applying remotely sensed data from instruments such as ASTER shows promise but warrants further development. In many of the classed remote sensing models, large areas classified as mainly one class have many sub-areas of other classes that consist of only a few pixels. These small areas may be caused by noise in the ASTER image or if they are real, are too small to be detected by AMS and NURE aerial surveys; thus, they add noise to the model. Further work into managing minimum pixel cluster sizes may lead to reducing this and lowering standard deviations, although it could force different subunits into the same class. The study area is also challenging. Cameron is very geologically diverse with many lithologic subunits that are relatively small. Further, the area is a U-mining district and as such the gamma-ray exposure rates over some portions of the Chinle Formation are not what would be considered typical. The use of remote sensing to aid modeling in more typical settings may prove a more powerful tool.

The predictive mapping process presented here provides a framework for application to other areas, especially in the continental US, Canada and other countries where large-scale gamma-ray surveys have been made. Factors such as increased vegetation and soil moisture should not affect the success of this strategy since even in temperate climates the radiological signature is still largely driven by bedrock geochemistry (e.g. Moxham, 1963; Griscom and Peterson, 1961; Beamish, 2013). The fact that the ANOVA F-statistic confirms that geologic units in our study area serve as effective background radiation units indicates that surface geochemistry is linked in a consistent way to bedrock geochemistry. Thus further investigation into how soil geochemistry evolves in various climates may lead to a method where bedrock geochemical analyses (combined with adequate geolocation information and metadata) can be used to predict gamma-ray background in areas where previous aerial surveys have not been conducted.

5. Conclusions

We have shown that in an arid environment within the contiguous 48 states, NURE aerial gamma-ray survey data sorted by geologic units may be used to create predictive models of the radiation background originating from geologic sources. Models based on geochemical data were less successful due to lack of sufficient data, sampling bias, and soil formation. Ongoing work on the relationship between radiation measurements and geochemical analysis may assist in improving these models. It is important to remember that our definition of success is extremely conservative. While some of these techniques may not fit within this narrow range of success, in the event of a nuclear disaster these techniques could still prove extremely useful. Further research and use of these techniques to model background radiation will allow for easier recognition of anomalies on aerial gamma-ray surveys, and thus location of valuable resources and hazards.

Acknowledgements

Appendix A. Supplementary data

Supplementary data related to this article can be found at http://dx.doi.org/10.1016/j.jenvrad.2016.07.012.

References

Abdeen, M.M., Allison, T.K., Abdelsalam, M.G., Stern, R.J., 2001. Application of ASTER band-ratio images for geological mapping in arid regions; the Neoproterozoic Allaqi Suture, Egypt. Abstr. Program Geol. Soc. Am. 3, 289.

Andrada de Palomera, R., 2002. Application of Remote Sensing and Geographic Information Systems for Mineral Predictive Mapping, Deseado Massif, Southern Argentina. Masters Thesis. International Institute for Geo-Information Science and Earth Observation, Enschede.

Andrada de Palomera, P., van Ruitenbeek, F.J.A., Carranza, E.J.M., 2015. Prospectivity for epithermal gold–silver deposits in the Deseado Massif, Argentina. Ore Geol. Rev. 71, 484–501.

Beamish, D., 2013. Gamma-ray attenuation in the soils of Northern Ireland, with special reference to peat. J. Environ. Radioact. 115, 13–27.

Beck, H., DeCampo, J., Gogolak, C., 1972. In-situ Ge(Li) and NaI(Tl) Gamma-ray Spectrometry, p. 75. Health and Safety Laboratory: No. HASL–258.

Billingsley, G.H., Priest, S.S., Felger, T.J., 2007. Geologic Map of the Cameron 30' × 60' Quadrangle, Coconino County, Northern Arizona. USGS Geological Survey.

Blumenthal, D.J., Musolino, S.V., 2016. International outdoor experiments and models for outdoor radiological dispersal devices. Health Phys. 110 (5), 401–402.

Blumenthal, D.J., Clark, H.W., Essex, J.J., Wagner, E.C., 2013. eFRMAC overview: data management and enabling technologies for characterization of a radiological release. Health Phys. 105 (1), 97–103.

Books, K.G., 1962. Aeroradioactivity survey and related surface geology of parts of the Los Angeles region, California (ARMS-I): biological and medical research division semiannual report: argonne national laboratory. Div. Biol. Med. Res. 59, 1–25.

Campbell, J.E., Klassen, R.A., Shives, R.B.K., 2007. Integrated field investigations of airborne radiometric data and drift composition, nuclear energy agency – international atomic energy agency Athabasca test area, Saskatchewan. EXTECH IV: geology and uranium EXploration TECHnology of the proterozoic Athabasca basin, Saskatchewan and Alberta. J. C.W. and D. G. Geol. Surv. Can. Bull. 588, 533–554.

Chen, X., Warner, T.A., Campagna, D.J., 2007. Integrating visible, near-infrared and short-wave infrared hyperspectral and multispectral thermal imagery for geological mapping at Cuprite, Nevada. Remote Sens. Environ. 110 (3), 344–356.

Damon, P.E., Shafiqullah, M., Leventhal, J.S., 1974. K-Ar chronology for the San Francisco volcanic field and rate of erosion of the Little Colorado River. In: Karlstrom, T.N.V., Swann, G.A., Eastwood, R.L. (Eds.), Geology of Northern Arizona with Notes on Archaeology and Paleoclimate; Part 1, Regional Studies and Field Guides: Geological Society of America, Rocky Mountain Section 27th Annual Meeting, Flagstaff, Ariz, pp. 220–235.

Di Tommaso, I., Rubinstein, N., 2007. Hydrothermal alteration mapping using ASTER data in the Infiernillo porphyry deposit, Argentina. Ore Geol. Rev. 32 (1), 275–290.

Dickson, B., 1995. Uranium-series disequilibrium in Australian soils and its effect on aerial gamma-ray surveys. J. Geochem. Explor. 54, 177–186. http://dx.doi.org/10.1016/0375-6742(95)00032-1.

Dickson, B.L., Scott, K.M., 1997. Interpretation of aerial gamma-ray surveys-adding the geochemical factors. AGSO J. Aust. Geol. Geophys. 17, 187–200.

Dierke, C., Werban, U., 2013. Relationships between gamma-ray data and soil properties at an agricultural test site. Geoderma 199, 90–98.

Dubiel, R.F., 1987. Sedimentology of the upper Triassic Chinle formation, southeastern Utah: paleoclimate implications. J. Arizona Nevada Acad. Sci. 22, 35–45.

Duval, J.S., Holman, P.B., Darnley, A.G., 2005. Terrestrial Radioactivity and Gamma-ray Exposure in the United States and Canada. Open-File Report 2005-1413. U.S. Geological Survey.

Ford, K., Keating, P., Thomas, M.D., 2007. Overview of geophysical signatures

associated with Canadian ore deposits. In: Goodfellow, W. (Ed.), Mineral Deposits of Canada: a Synthesis of Major Deposit- Types, District Metallogeny, the Evolution of Geological Provinces, and Exploration Methods. Geological Association of Canada, Mineral Deposits Division, pp. 939–970. Special Publication No. 5.

Ford, K., Harris, J.R., Shives, R., Carson, J., Buckle, J., 2008. Remote predictive mapping 2: gamma-ray spectrometry: a tool for mapping Canada's north. Geosci. Can. 35 (3–4), 109–126.

Gad, S., Kusky, T., 2007. ASTER spectral ratioing for lithological mapping in the Arabian–Nubian shield, the Neoproterozoic Wadi Kid area, Sinai, Egypt. Gondwana Res. 11 (3), 326–335.

Galbraith, J.H., Saunders, D.F., 1983. Rock classification by characteristics of aerial gamma-ray measurements. J. Geochem. Explor. 18, 49–73.

Grasty, R., Carson, J., Charbonneau, B., Holman, P., 1984. Natural background radiation in Canada. Geol. Surv. Can. Bull. 360, 39.

Griscom, A., Peterson, D.L., 1961. Aeromagnetic, aeroradioactivity, and gravity investigations of Piedmont rocks in the Rockville quadrangle, Maryland. U. S. Geol. Surv. Prof. Pap. D267–D271.

Harris, J., 1989. In: Agterberg, F.P., Bonham-Carter, G.F. (Eds.), Clustering of Gamma Ray Spectrometer Data Uinsg a Computer Image Analysis System, Statistical Applications in the Earth Sciences, pp. 19–31.

Hendricks, T.J., 2001. An Aerial Radiological Survey of Abandoned Uranium Mines in the Navajo Nation. Report for Bechtel Nevada Remote Sensing Laboratory. U.S. Department of Energy, p. 24. DOE/NV/11718–602.

Hewson, R., Cudahy, T., 2011. Issues affecting geological mapping with ASTER data, a case study of the Mt Fitton area, south Australia. In: Ramachandran, B., Justice, C.O., Abrams, M.J. (Eds.), Land Remote Sensing and Global Environmental Change: NASA's Earth Observing System and the Science of ASTER and MODIS. Springer, New York, pp. 273–300.

Hopkins, R.L., Thompson, K.L., 2003. Kiabab formation. In: Beus, S.S., Morales, M. (Eds.), Grand Canyon Geology, 2nd. Oxford University Press, New York, ISBN 978-0-19-512299-2, pp. 196–211. 448 pp.

IAEA-TECDOC 1363, 2003. Guidelines for Radioelement Mapping Using Gamma Ray Spectrometry Data. International Atomic Energy Agency, Vienna.

Jones, D., 2004. Airborne Measurement of Radioactivity. For Geological and Environmental Monitoring. Earthwise, British Geological Survey, NERC, pp. 8–9.

Koons, R.D., Helmke, P.A., Jackson, M.L., 1980. Association of trace elements with iron oxides during rock weathering. Soil Sci. Soc. Am. J. 44, 155–159.

Lehnert, K., 2016. EarthChem Portal Home | EarthChem. Earthchem.org.

Løvborg, L., Kirkegaard, P., 1974. Response of 3″ × 3″ NaI(Tl) detectors to terrestrial gamma radiation. Nucl. Instrum. Methods 121, 239–251. http://dx.doi.org/10.1016/0029-554x(74)90072-x.

Lyons, C., Colton, D., 2012. Aerial measuring system in Japan. Health Phys. 102 (5), 509–515.

Mars, J.C., Rowan, L.C., 2006. Regional mapping of phyllic-and argillic-altered rocks in the Zagros magmatic arc, Iran, using advanced spaceborne thermal emission and reflection radiometer (ASTER) data and logical operator algorithms. Geosphere 161–186.

Martelet, G., Truffert, C., Tourliere, B., Ledru, P., Perrin, J., 2006. Classifying airborne radiometry data with Agglomerative Hierarchical Clustering: a tool for geological mapping in context of rainforest (French Guiana). Int. J. Appl. Earth Obs. Geoinf. 8, 208–223.

Martz, L.W., deJong, E., 1990. Natural radionuclides in the soils of a small agricultural basin in the canadian prairies and their association with topography, soil properties and erosion. Catena 17 (1), 85–96.

McWilliam, N., Teeuw, R., Whiteside, M., Zukowskyj, P., 2005. GIS GPS and Remote Sensing: Field Techniques Manual, in Chapter 8: Image Interpretation and Processing. Royal Geography Society, London, p. 148.

Mernagh, T.P., Miezitis, Y., 2008. A Review of the Geochemical Processes Controlling the Distribution of Th in the Earth's Crust and Australia's Th Resources, p. 48.

Geoscience Australia Record 2008/05.

Minty, B., 1997. Fundamentals of airborne gamma-ray spectrometry. AGSO J. Aust. Geol. Geophys. 17, 39–50.

Moxham, R., 1963. Natural radioactivity in Washington county, Maryland. Geophysics 28, 262–272. http://dx.doi.org/10.1190/1.1439174.

Pickup, G., Marks, A., 2000. Identifying large-scale erosion and deposition processes from airborne gamma radiometrics and digital elevation models in a weathered landscape. Earth Surf. Process. Landforms 25 (5), 535–557.

Pitkin, J., Bates, R., Neuschel, S., 1964. Aeroradioactivity surveys and geologic mapping (Nuclear facility background gamma radiation measured by aerial radiological measurement). Nat. Radiat. Environ. 723–736.

Pour, A.B., Hashim, M., 2012. The application of ASTER remote sensing data to porphyry copper and epithermal gold deposits. Ore Geol. Rev. 44, 1–9.

Rawlins, B.G., Lark, R.M., Webster, R., 2007. Understanding airborne radiometric survey signals across part of eastern England. Earth Surf. Process. Landforms 32, 1503–1515.

Rowan, L.C., Mars, J.C., 2003. Lithologic mapping in the Mountain Pass, California area using advanced spaceborne thermal emission and reflection radiometer (ASTER) data. Remote Sens. Environ. 84 (3), 350–366.

Rowan, L.C., Hook, S.J., Abrams, M.J., Mars, J.C., 2003. Mapping hydrothermally altered rocks at Cuprite, Nevada, using the advanced spaceborne thermal emission and reflection radiometer (ASTER), a new satellite-imaging system. Econ. Geol. 98 (5), 1019–1027.

Rowan, L.C., Mars, J.C., Simpson, C.J., 2005. Lithologic mapping of the mordor, NT, Australia ultramafic complex by using the advanced spaceborne thermal emission and reflection radiometer (ASTER). Remote Sens. Environ. 99, 105–126.

Sanada, Y., Sugita, T., Nishizawa, Y., Kondo, A., Torii, T., 2014. The aerial radiation monitoring in Japan after the Fukushima Daiichi nuclear power plant accident. Prog. Nucl. Sci. Technol. 4, 76–80.

Sanderson, D., Allyson, J.D., Tyler, A.N., Ni Riain, S., Murphy, S., 1993. An Airborne Gamma Ray Survey of Parts of SW Scotland in February 1993. Final Report. Project Report. Scottish Universities Research and Reactor Centre, Glasgow, UK. http://eprints.gla.ac.uk/59483/.

Sanderson, D.C.W., Cresswell, A.J., Hardeman, F., Debauche, A., 2004. An airborne gamma-ray spectrometry survey of nuclear sites in Belgium. J. Environ. Radioact. 72 (1–2), 213–224.

Sarbas, B., 2008. The GEOROC database as part of a growing geoinformatics network. In: Brady, S.R., Sinha, A.K., Gundersen, L.C. (Eds.), Geoinformatics 2008—Data to Knowledge, pp. 42–43. Proceedings: U.S. Geological Survey Scientific Investigations Report 2008-5172.

Schetselaar, E.M., Rencz, A.N., 1997. Reducing the effects of vegetation cover on airborne radiometric data using Landsat TM data. Int. J. Remote Sens. 18, 1503–1515.

Schetselaar, E.M., Chung, C.J.F., Kim, K.E., 2000. Integration of Landsat TM, gamma-ray, magnetic, and field data to discriminate lithological units in vegetated granite-gneiss terrain. Remote Sens. Environ. 71, 89–105.

Sigleo, A., 1979. Geochemistry of silicified wood and associated sediments, petrified forest national park, Arizona. Chem. Geol. 26, 151–163. http://dx.doi.org/10.1016/0009-2541(79)90036-6.

Ulrich, G.E., Bailey, N.G., 1987. Geologic Map of the S P Mountain Part of the San Francisco Volcanic Field, Northcentral Arizona. U.S. Geological Survey Miscellaneous Field Studies Map MF–1956, scale 1:50, 000, 2 sheets.

van der Meer, F., van der Werff, H., van Ruitenbeek, F., Hecker, C., Bakker, W., Noomen, M., van der Meijde, M., Carranza, E., Smeth, J., Woldai, T., 2012. Multi-and hyperspectral geologic remote sensing: a review. Int. J. Appl. Earth Obs. Geoinf. 14, 112–128. http://dx.doi.org/10.1016/j.jag.2011.08.002.

Wilford, J., 2002. In: Papp, E. (Ed.), Airborne Gamma-ray Spectrometry. Geophysical and Remote Sensing Methods for Regolith Exploration, pp. 46–52. CRCLEME Open File Report 114.